

Bayesian Transfer Learning for Artificially Intelligent Geospatial Systems: A Predictive Stacking Approach

Luca Presicce^a and Sudipto Banerjee^b

^a Department of Economics, Management and Statistics,
Università degli studi Milano-Bicocca, Milano, Italy

^bDepartment of Biostatistics,
University of California Los Angeles, CA, USA.

Abstract

Building artificially intelligent geospatial systems requires rapid delivery of spatial data analysis on massive scales with minimal human intervention. Depending upon their intended use, data analysis can also involve model assessment and uncertainty quantification. This article devises transfer learning frameworks for deployment in artificially intelligent systems, where a massive data set is split into smaller data sets that stream into the analytical framework to propagate learning and assimilate inference for the entire data set. Specifically, we introduce Bayesian predictive stacking for multivariate spatial data and demonstrate rapid and automated analysis of massive data sets. Furthermore, inference is delivered without human intervention without excessively demanding hardware settings. We illustrate the effectiveness of our approach through extensive simulation experiments and in producing inference from massive dataset on vegetation index that are indistinguishable from traditional (and more expensive) statistical approaches.

Keywords— Bayesian predictive stacking; Climate science; Gaussian process; Geospatial systems; Matrix-variate spatial models; Transfer learning.

1 Introduction

Geospatial artificial intelligence (GEOAI) is a rapidly evolving discipline at the interface of machine learning and spatial data science that attempts to harness the analytical capabilities of Artificial Intelligence (AI) to analyze massive amounts of geographic data for data driven scientific discoveries in the environmental and physical sciences. The area, while still fledgling, presents opportunities for statisticians to devise essential data analytic tools that

should comprise an artificially intelligent “geospatial” system. This manuscript concerns itself primarily with statistical learning tools for artificially intelligent GEOAI systems.

What should be the role of statistical inference in GEOAI? Formal inference for spatial random fields enjoy a venerable intellectual presence spanning several decades of theoretical developments within classical and Bayesian paradigms (see, e.g., [Cressie, 1993](#); [Stein, 1999](#); [Gelfand et al., 2010](#); [Cressie and Wikle, 2011](#); [Banerjee et al., 2015](#)). Statisticians have built richly structured hierarchical models in pursuit of “full” probabilistic inference for richly structured spatial data. The term “full” loosely refers to approaches that estimate *all* unknowns in the model including all parameters (irrespective of how well they are informed by the data), random effects, and predictive random variables for probabilistic interpolation at arbitrary locations (and time points in spatial-temporal data).

Spatial modeling relies upon Gaussian processes (GPs) to model dependence and achieves superior predictive inference. While GPs afford flexibility and are a conspicuous choice in spatial modeling, they do not generally offer computationally exploitable structures for covariance matrices. The computational requirements for full inference become onerous and impracticable for massive datasets. This presents a conundrum: should we strive to completely retain the probabilistic rigors of theoretical inference, which may be computationally burdensome, or even impracticable, given the massive amounts of data, or should we concede uncertainty quantification and adopt algorithm-driven data analysis that would easily scale massive data sets? Spatial data analysis at unprecedented scales requires some concessions from conventional decision-theoretic paradigms as has been reflected, for example, in a recent comprehensive case study by [Zhou et al. \(2022\)](#), who synthesize statistical models with machine learning algorithms to measure temporal trends and spatial distribution of housing vitality by exploiting information from multiple sources (also see the discussion by [Banerjee, 2022](#), for conventional Bayesian modeling perspectives and its challenges). Other efforts in melding machine learning methods with formal spatial statistics include deep learning for

spatial data (Zammit-Mangion et al., 2022; Wikle and Zammit-Mangion, 2023, with the latter offering a comprehensive review of spatial machine learning) and, in a very related domain, for deep GP emulation in computer experiments (Sauer et al., 2023b), and spatial random forests (Georganos et al., 2021; Talebi et al., 2022; Saha et al., 2023).

Even a cursory review reveals a significant literature on methods for massive spatial datasets, which is too vast to be summarized here (see, e.g., Banerjee, 2017; Heaton et al., 2017). In hierarchical models $[data \mid process] \times [process \mid parameters] \times [parameters]$, inference proceeds from spatial processes that scale massive data sets. Examples range from reduced-rank or subsets of regression approaches (see, e.g., Quiñonero-Candela and Rasmussen, 2005; Cressie and Johannesson, 2008; Banerjee et al., 2008; Wikle, 2010), multi-resolution approaches (Nychka et al., 2015; Katzfuss, 2017), and graph-based models Vecchia (1988); Datta et al. (2016); Katzfuss and Guinness (2021); Dey et al. (2022); Sauer et al. (2023a). Full inference typically requires Markov chain Monte Carlo (MCMC) (Finley et al., 2019), variational approximations (Ren et al., 2011; Wu et al., 2022; Cao et al., 2023) and a significant body of literature on Gaussian Markov random field approximations (Rue et al., 2009; Lindgren et al., 2011) in conjunction with integrated nested Laplace approximations (INLA) for computing the marginal distributions of the process at given locations.

The aforementioned methods focus upon richness of statistical inference, but almost invariably involve a significant amount of human intervention to analyze spatial data. Even the simplest geostatistical data require exploratory data analysis to learn about aspects of the underlying process that are weakly identified by the data (Zhang, 2004; Tang et al., 2021). Building a GEOAI system, on the other hand, will require minimizing human intervention in offering a robust framework for spatial data analysis. This presents enough challenges that preclude a comprehensive solution in its entirety within the scope of a single manuscript. Nevertheless, we devise a spatial data analytic framework that holds significant promise for GEOAI. The premise of this approach relies upon two basic tenets: (i) model-based statistical

inference for underlying spatial processes (including multivariate processes) in a robust and largely automated manner with minimal human input; and (ii) achieving such inference for truly massive amounts of data without resorting to iterative algorithms that may require significant human intervention to diagnose convergence (such as in MCMC).

We retain the benefits of posterior learning of the underlying stochastic process. In particular, we obtain predictive inference over the uncountable collection of points in the spatial domain while propagating uncertainty about the model’s estimation in such inference. However, some compromises with regard to richness of models are inevitable from the standpoint of GEOAI. At the same time, statistical distribution theory has much to offer and we harness analytical closed-form distribution theory within a family of matrix-variate distributions to deliver inference. This is possible only by “fixing” certain spatial correlation kernel parameters that are weakly identified and hinder automated inference. We execute fast and exact inference based upon the matrix-variate distributions and then assimilate the inference using Bayesian predictive stacking or BPS ([Wolpert, 1992](#); [Yao et al., 2018](#)). Stacking ([Breiman, 1996](#)) is primarily related to predictions by minimizing the generalization error rate of one or more models. Bayesian predictive stacking (BPS) is a particular type of Bayesian predictive synthesis (see, e.g., [Yao et al., 2018](#); [McAlinn and West, 2019](#); [McAlinn et al., 2020](#); [Tallman and West, 2023](#); [Cabel et al., 2025](#), for different perspectives).

A GEOAI system will access massive amounts of data. We devise Bayesian transfer learning over a streaming set of spatial datasets. The data streams into the GEOAI system in the form of K subsets, each with $\approx n/K$ locations. We analyze and propagate inference from one subset to the next and assimilate inference from these subsets. Delegating Bayesian calculations to a group of independent datasets is intuitive and has been explored from diverse perspectives. Examples include Consensus Monte Carlo (CMC) ([Scott et al., 2016](#)) and its kernel-based adaptations ([Rendell et al., 2021](#)), Bayesian meta-analysis in clinical applications (see, e.g., Chapter 4 in [Parmigiani, 2002](#)) and in spatially-temporally structured

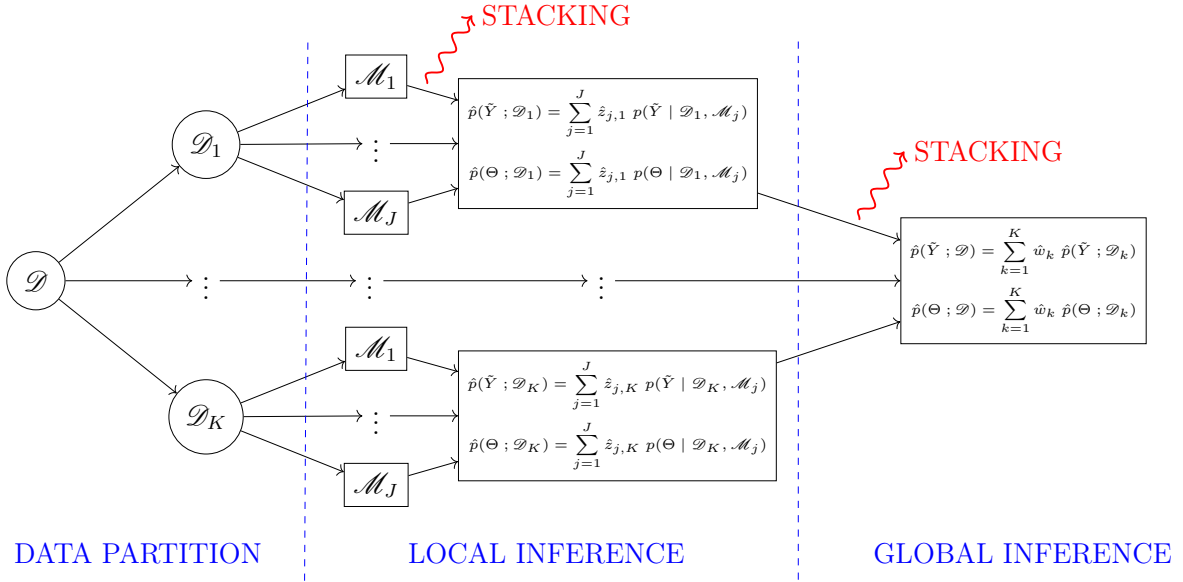


Figure 1: Double Bayesian predictive stacking approach representation

data (Bell et al., 2005; Kang et al., 2011); and, more recently, “meta” approaches using diverse distributed computing architectures (Srivastava et al., 2015; Deisenroth and Ng, 2015; Minsker et al., 2017; Srivastava et al., 2018; Guhaniyogi and Banerjee, 2018, 2019; Guhaniyogi et al., 2019, 2022, 2023). Most approaches have relied on iterative algorithms for estimating weakly identifiable parameters. We propose transfer learning using a double stacking approach. We first obtain stacked inference for each of the parameters within each subset and, then, assimilate inference across subsets by a second stacking algorithm. A flowchart is supplied in Figure 1 comprising three steps: (i) partition data into smaller subsets; (ii) analyze each subset by stacking conjugate posteriors in closed form; and (iii) stack across data sets to deliver inference for the entire data.

This article evolves according to Figure 1. Section 2 outlines Bayesian transfer learning using DOUBLE BPS (DBPS), Section 3 provides details on computation, Section 4 presents simulation experiments to illustrate and evaluate DOUBLE BPS and its applicability to amortized inference. Section 5 analyzes a vegetation index data set with observed locations in the millions on global scales. Finally, Section 6 concludes with some discussion. References to an accompanying Supplement are provided throughout the article and after Section 6.

2 Bayesian transfer learning

Transfer learning (TL) broadly refers to propagating knowledge from one task to accomplish a different task (see [Suder et al., 2023](#), and references therein). We devise transferring inference from one subset to the next in a stream of subsets to analyze the entire dataset. Learning from spatial random fields is challenging because of limited information available for the latent spatial process (uncountable collection of unobserved random variables) using a partially observed finite realization. We develop an automated approach for GEOAI.

2.1 Divide-and-Conquer Multivariate Bayesian inference

Let $Y_{n \times q}$ be an $n \times q$ random matrix that is endowed with a probability law from the matrix-normal distribution, $\text{MN}(M, V, U)$, with probability density function

$$p(Y \mid M, V, U) = \frac{\exp \left[-\frac{1}{2} \text{tr} \{ U^{-1} (Y - M)^T V^{-1} (Y - M) \} \right]}{(2\pi)^{\frac{np}{2}} |U|^{\frac{n}{2}} |V|^{\frac{q}{2}}}, \quad (2.1)$$

where $\text{tr}(\cdot)$ is the trace operator on a square matrix, M is the mean matrix, and V and U are the $n \times n$ row-covariance and $q \times q$ column covariance matrices, respectively. We consider the matrix-variate Bayesian linear regression model

$$Y = X\beta + E_Y, \quad E_Y \sim \text{MN}(O, V, \Sigma); \quad \beta = M_0 m_0 + E_\beta, \quad E_\beta \sim \text{MN}(O, M_0, \Sigma), \quad (2.2)$$

where Y is $n \times q$, X is $n \times p$ comprising explanatory variables, β is $p \times q$ consisting of regression slopes, E_Y and E_β are zero-centered random matrices with row covariances V and M_0 , respectively, and a shared column covariance matrix Σ . We assign an inverse-Wishart distribution $\Sigma \sim \text{IW}(\Psi_0, \nu_0)$ and denote the joint density of β and Σ by $\text{MNIW}(M_0 m_0, M_0, \Psi_0, \nu_0)$, which affords a closed-form posterior for $\{\beta, \Sigma\}$ in the same family.

Let $\mathcal{D} = \{Y, X\}$ be the entire dataset, which is too massive to even be accessed, let alone be analyzed using (2.1), within the GEOAI system. Therefore, we envisage K disjoint and exhaustive subsets $\mathcal{D} = \{\mathcal{D}_1, \dots, \mathcal{D}_K\}$ streaming into GEOAI as a sequence. Each $\mathcal{D}_k = \{Y_k, X_k\}$ consists of n_k rows of Y and X , where $n = \sum_{k=1}^K n_k$, Y_k is $n_k \times q$ and X_k is $n_k \times p$ for each $k = 1, \dots, K$. We now fit (2.2) to each subset using $Y_k = X_k\beta + E_k$, $E_k \sim \text{MN}(O, V_k, \Sigma)$, where V_k is the $n_k \times n_k$ row-covariance matrix corresponding to the rows in Y_k ; the specification for $\{\beta, \Sigma\}$ remains as in (2.2). Starting with $\text{MNIW}(\beta, \Sigma | M_k m_k, M_k, \Psi_k, \nu_k)$ at $k = 0$ (the prior), we use Bayesian updating $p(\beta, \Sigma | \mathcal{D}_{1:k+1}) \propto p(\beta, \Sigma | \mathcal{D}_{1:k}) \times p(Y_{k+1} | X_{k+1}\beta, V_{k+1}, \Sigma)$ to obtain $\beta, \Sigma | \mathcal{D}_{1:k+1} \sim \text{MNIW}(M_{k+1} m_{k+1}, M_{k+1}, \Psi_{k+1}, \nu_{k+1})$ with $M_{k+1}^{-1} = M_k^{-1} + X_{k+1}^T V_{k+1}^{-1} X_{k+1}$, $m_{k+1} = m_k + X_{k+1}^T V_{k+1}^{-1} Y_{k+1}$, $\nu_{k+1} = \nu_k + n_{k+1}$, and $\Psi_{k+1} = \Psi_k + Y_{k+1}^T V_{k+1}^{-1} Y_{k+1} + m_k^T M_k m_k - m_{k+1}^T M_{k+1} m_{k+1}$. Upon termination at $k = K$, we exactly recover the posterior distribution $p(\beta, \Sigma | \mathcal{D})$. There is no need to interact between the subsets, and computational complexity is determined solely by the dimension of the subsets.

Spatial random fields immediately present a challenge. The above method delivers inference without loss of information only if Y_k 's are independent between blocks. If each row of Y corresponds to a spatial location so V is an $n \times n$ spatial correlation matrix, then each V_k is the spatial correlation matrix constructed from n_k spatial locations in \mathcal{D}_k . The independence among K blocks may yield reasonable inference if we can design the blocks such that the spatial correlation between blocks does not impact the general inference. However, designing such blocks requires significant human intervention. We seek to avoid this in GEOAI.

Instead, we assimilate statistical learning from each of these blocks using predictive stacking. We exploit the fact that V is indexed by a small number of parameters in a spatial correlation kernel. Fixing these parameters fixes V , and hence V_k for each k , producing closed-form posterior inference on β and Σ based on the entire dataset as described above. Stacking combines these analytically accessible distributions using an optimal set of weights that are computed using a convex optimization algorithm. These weights are then used to

reconstruct the posterior and predictive distributions for the spatial random field without imposing block independence. Existing “meta-kriging” and related “divide and conquer” approaches (e.g., [Guhaniyogi and Banerjee, 2018](#); [Scott et al., 2016](#), and other references on “divide and conquer” methods provided in Section 1) analyze subsets of data using MCMC, which is expensive and not fully automated. A key distinction of the current manuscript is that we abandon all iterative estimation algorithms, let alone expensive MCMC, and focus on assimilating inference using closed forms of distributions.

What remains to be resolved is the issue of fixing the parameters in V . These parameters govern the strength of association across the spatial random field and possibly the smoothness of the field. Unfortunately, these parameters are weakly identified by the data and posterior learning struggles due to slower convergence of iterative algorithms. Also, exploratory spatial data science tools, such as variograms, for gleaning information about these parameters will also be less helpful as they may suggest different values for each of the variables indexed by the columns, while we insist on retaining a single parameter to exploit conjugate distribution theory. Hence, we collect the closed-form posterior distributions obtained for a collection of fixed values of the spatial parameters and, subsequently, average these posterior distributions.

2.2 Bayesian stacking of predictive densities

Bayesian predictive stacking (BPS) assimilates models using a weighted distribution in the convex hull, $C = \left\{ \sum_{j=1}^J w_j p(\cdot \mid \mathcal{D}, \mathcal{M}_j) : \sum_j w_j = 1, w_j \geq 0 \right\}$, of individual posterior distributions by maximizing the score ([Gneiting and Raftery, 2007](#); [Yao et al., 2018](#)) to fetch

$$(w_1, \dots, w_J)^T = \arg \max_{w \in S_1^J} \frac{1}{n} \sum_{i=1}^n \log \sum_{j=1}^J w_j p(Y_i \mid \mathcal{D}_{-i}, \mathcal{M}_j) , \quad (2.3)$$

where \mathcal{D}_{-i} is the dataset excluding the i -th block (indexed by a row) of observations in Y , and $\mathcal{M} = (\mathcal{M}_1, \dots, \mathcal{M}_J)$ are J different models. For any given dataset \mathcal{D} , these J different models correspond to fixed spatial correlation kernel parameters in V and deliver closed-form

analytic distributions. Solving (2.3) minimizes the Kullback-Leibler divergence from the true predictive distribution using convex optimization (Grant and Boyd, 2008; Fu et al., 2020). While the true predictive distribution is unknown, we use a leave-one-out (LOO) estimate of the expected value of the score (see. e.g., Yao et al., 2018, for details), which requires fitting the model n times as we exclude one row of the data \mathcal{D} at a time. We prefer K-fold cross-validation as a more cost-effective method for generating predictions (Breiman, 1996).

2.3 Accelerated learning for spatial random fields

Let $\mathcal{S} = \{s_1, \dots, s_n\} \subset \mathcal{D}$ be a set of n locations yielding observations on q possibly correlated outcomes collected into a $q \times 1$ vector $y(s) = (y_1(s), \dots, y_q(s))^T$ for each $s \in \mathcal{S}$. We collect these measurements into the $n \times q$ matrix $Y = [y_j(s_i)^T]$ for $i = 1, \dots, n$ and $j = 1, \dots, q$. Let $X = [x(s_i)^T]$ be $n \times p$ with rows $x(s_i)^T$ consisting of $p < n$ explanatory variables at location $s_i \in \mathcal{S}$; we assume X has rank p . We introduce latent spatial processes, $\omega_j(s)$, for each outcome $y_j(s)$ to capture spatial dependence and a $q \times q$ covariance matrix, Σ , to capture non-spatial dependence among the elements of $y(s)$ within s . This matrix is typically adjusted by a scale factor $(\alpha^{-1} - 1)$ to accommodate additional variation at local scales. For example, setting $\alpha = \sigma^2 / (\sigma^2 + \tau^2)$ where σ^2 and τ^2 denote variances for the spatial process and measurement error (“nugget”) implies α is the ratio of the spatial variance (partial sill) to the total variance (sill) gleaned from a variogram in classical geostatistics.

We cast this into (2.2), but explicitly introduce a latent $q \times 1$ spatial process $\omega(s)$ as

$$\begin{aligned} Y &= X\beta + \Omega + E, \quad E \mid \Sigma \sim \text{MN}(O, (\alpha^{-1} - 1)\mathbb{I}_n, \Sigma); \quad \Sigma \sim \text{IW}(\Psi_0, \nu_0); \\ \beta &= M_0 m_0 + E_\beta, \quad E_\beta \mid \Sigma \sim \text{MN}(O, M_0, \Sigma); \quad \Omega \mid \Sigma \sim \text{MN}(O, V, \Sigma), \end{aligned} \tag{2.4}$$

where $\Omega = [\omega(s_i)^T]$ is $n \times q$ with rows $\omega(s_i)^T$. To capture spatial dependence, V is an $n \times n$ spatial correlation matrix with (i, j) -th element equaling the value of a positive definite spatial correlation function $\rho(s_i, s_j; \phi)$ indexed by parameter(s) ϕ . To account for measurement

errors in observations, as is customary in geostatistics, we introduce a discontinuity in the spatial correlation function and modify the elements to $\rho(s_i, s_j; \phi) + (\alpha^{-1} - 1)\mathbb{1}_{s_i=s_j}$, where $\alpha \in [0, 1]$ represents the proportion of total variability attributed to the spatial process.

Letting $\gamma^T = [\beta^T, \Omega^T]$ be $q \times (p + n)$, we assume $\{\gamma, \Sigma\} \sim \text{MNIW}(\mu_\gamma, V_\gamma, \Psi_0, \nu_0)$, where

$$\text{MNIW}(\gamma, \Sigma \mid \mu_\gamma, V_\gamma, \Psi_0, \nu_0) = \text{IW}(\Sigma \mid \Psi_0, \nu_0) \times \text{MN}_{p,q}(\gamma \mid \mu_\gamma V_\gamma, \Sigma), \quad (2.5)$$

with $\mu_\gamma^T = [m_0^T M_0, 0_{q \times n}]$ and $V_\gamma = \text{blockdiag}\{M_0, \rho_\phi(\mathcal{S}, \mathcal{S})\}$. The MNIW prior is conjugate with respect to the matrix-normal likelihood. Thus, for any fixed $\{\alpha, \phi\}$ and hyperparameters in the prior density, we obtain a MNIW posterior density for $\{\gamma, \Sigma\}$,

$$p(\gamma, \Sigma \mid \mathcal{D}) = \text{MNIW}(\gamma, \Sigma \mid \mu_\gamma^*, V_\gamma^*, \Psi^*, \nu^*), \quad (2.6)$$

where $V_\gamma^* = \begin{bmatrix} \frac{\alpha}{1-\alpha} X^T X + M_0^{-1} & \frac{\alpha}{1-\alpha} X^T \\ \frac{\alpha}{1-\alpha} X & \rho_\phi^{-1}(\mathcal{S}, \mathcal{S}) + \frac{\alpha}{1-\alpha} \mathbb{I}_n \end{bmatrix}^{-1}$ and $\mu_\gamma^* = V_\gamma^* \begin{bmatrix} \frac{\alpha}{1-\alpha} X^T Y + m_0 \\ \frac{\alpha}{1-\alpha} Y \end{bmatrix}$, $\Psi^* = \Psi_0 + \frac{\alpha}{1-\alpha} Y^T Y + m_0^T M_0 m_0 - \mu_\gamma^{*T} V_\gamma^{*-1} \mu_\gamma^*$ and $\nu^* = \nu_0 + n$.

The framework in (2.4) is equivalent to (2.2) with $V = R_\phi + (\alpha^{-1} - 1)\mathbb{I}_n$ with $R_\phi = [\rho(s_i, s_j; \phi)]$. We recover posterior samples of Ω by drawing a value of Ω from $p(\Omega \mid \mathcal{D}, \beta, \Sigma, \mathcal{M}_j)$ for every posterior draw of $\{\beta, \Sigma\}$. This renders itself seamlessly to the Bayesian transfer learning framework described in Section 2.1 provided that V , or $\{\alpha, \phi\}$, is fixed. For GEOAI, we seek to minimize human intervention. Rather than fixing them at one particular value, perhaps gleaned from a spatial variogram that requires human inspection, we use a set of J candidate values $\{\alpha_j, \phi_j\}$ specifying model \mathcal{M}_j for $j = 1, \dots, J$. We now obtain analytical closed forms for $p(\beta, \Sigma \mid \mathcal{D}, \mathcal{M}_j)$ for each j , as described in Section 2.1, and use Bayesian predictive stacking to evaluate the stacked posterior distribution.

Turning to prediction, let $\mathcal{U} = \{u_1, \dots, u_{n'}\}$ be a finite set of locations where we seek to predict or impute the value of Y based upon an observed $n' \times p$ design matrix $X_{\mathcal{U}}$ associated with the locations in \mathcal{U} . The joint posterior predictive for $Y_{\mathcal{U}}$ and the unobserved latent

process $\Omega_{\mathcal{U}} = [\omega(u_i)^T]$ for $i = 1, \dots, n'$, can be recast by integrating out $\{\gamma, \Sigma\}$ from the conditional posterior predictive distribution to yield

$$\begin{aligned} p(Y_{\mathcal{U}}, \Omega_{\mathcal{U}} \mid \mathcal{D}) &= \int \text{MN}_{n',q}(Y_{\mathcal{U}} \mid X_{\mathcal{U}}\beta + \Omega_{\mathcal{U}}, (\alpha^{-1} - 1)\mathbb{I}_{n'}, \Sigma) \\ &\quad \times \text{MN}_{n',q}(\Omega_{\mathcal{U}} \mid M_{\mathcal{U}}\Omega, V_{\Omega_{\mathcal{U}}}, \Sigma) \times \text{MNIW}(\gamma, \Sigma \mid \mu_{\gamma}^*, V_{\gamma}^*, \Psi^*, \nu^*) d\gamma d\Sigma, \end{aligned} \quad (2.7)$$

where $M_{\mathcal{U}} = \rho_{\phi}(\mathcal{U}, \mathcal{S})\rho_{\phi}^{-1}(\mathcal{S}, \mathcal{S})$ and $V_{\Omega_{\mathcal{U}}} = \rho_{\phi}(\mathcal{U}, \mathcal{U}) - \rho_{\phi}(\mathcal{U}, \mathcal{S})\rho_{\phi}^{-1}(\mathcal{S}, \mathcal{S})\rho_{\phi}(\mathcal{S}, \mathcal{U})$. This is a matrix-variate Student's t $T_{2n',q}(\nu^*, \mu^*, V^*, \Psi^*)$, with degrees of freedom ν^* , location matrix $\mu^* = M\mu_{\gamma}^*$, row-scale matrix V^* , and column-scale matrix Ψ^* , where $M = \begin{bmatrix} 0 & M_{\mathcal{U}} \\ X_{\mathcal{U}} & M_{\mathcal{U}} \end{bmatrix}$ and $V^* = MV_{\gamma}^*M^T + V_E$ with $V_E = \begin{bmatrix} V_{\Omega_{\mathcal{U}}} & V_{\Omega_{\mathcal{U}}} \\ V_{\Omega_{\mathcal{U}}} & V_{\Omega_{\mathcal{U}}} + (\alpha^{-1} - 1)\mathbb{I}_{n'} \end{bmatrix}$. See Section S2.1 for details. While the conditional posterior predictive distributions take the following forms

$p(\Omega_{\mathcal{U}} \mid \mathcal{D}, \gamma, \Sigma) = \text{MN}_{n',q}(\Omega_{\mathcal{U}} \mid M_{\mathcal{U}}\Omega, V_{\Omega_{\mathcal{U}}}, \Sigma)$, and $p(Y_{\mathcal{U}} \mid \mathcal{D}, \Omega_{\mathcal{U}}, \gamma, \Sigma) = \text{MN}_{n',q}(Y_{\mathcal{U}} \mid X_{\mathcal{U}}\beta + \Omega_{\mathcal{U}}, (\alpha^{-1} - 1)\mathbb{I}_{n'}, \Sigma)$. Hence, we can proceed with posterior predictive inference by sampling from the closed-form joint predictive distribution or sampling from the conditional distributions. We draw one instance of $\Omega_{\mathcal{U}} \sim p(\Omega_{\mathcal{U}} \mid \mathcal{D}, \gamma, \Sigma)$ for each posterior draw of $\{\gamma, \Sigma\}$ and then draw one value of $Y_{\mathcal{U}} \sim p(Y_{\mathcal{U}} \mid \mathcal{D}, \Omega_{\mathcal{U}}, \gamma, \Sigma)$ for each drawn $\{\Omega_{\mathcal{U}}, \gamma, \Sigma\}$. The resulting samples are exactly drawn from the posterior predictive distribution $p(Y_{\mathcal{U}} \mid \mathcal{D})$.

This tractability is possible if the range decay ϕ and α are fixed. While data can inform about these parameters, they are inconsistently estimable and lead to poorer convergence (Zhang, 2004). Finley et al. (2019) explored K -fold cross-validation, but inference is limited to only one set of values for the parameters. Instead, we pursue exact inference using (2.6) and (2.7) by stacking over different fixed values of $\{\alpha, \phi\}$ using BPS of predictive densities as described in Section 2.2. This minimizes human intervention and enables automation.

For each subset of the data we compute the stacking weights $z_k = \{z_{k,j}\}_{j=1,\dots,J}$ as

$$\max_{z_k \in S_1^J} \frac{1}{n_k} \sum_{i=1}^{n_k} \log \sum_{j=1}^J z_{k,j} p(Y_{k,i} \mid \mathcal{D}_{k,[-l]}, \mathcal{M}_j), \quad (2.8)$$

where $Y_{k,i}$ is the i -th of the n_k rows of $Y_{k,[l]} \in \mathcal{D}_{k,[l]}$ (the l -th fold within the k -th dataset), and $\mathcal{D}_{k,[-l]}$ is the k -th dataset without the l -th fold, with $l = 1, \dots, L$, and L the number of folds for K-fold cross-validation estimates for the expected value of the score (see Section 2.2). The posterior predictive density, $p(Y_{k,i} | \mathcal{D}_{k,[-l]}, \mathcal{M}_j)$, is available in closed form as a matrix t distribution, which makes the computation efficient. Leading Equation (2.8) to

$$\max_{z_k \in S_1^J} \frac{1}{n_k} \sum_{i=1}^{n_k} \log \sum_{j=1}^J z_{k,j} T_{1,q}(Y_{k,i} | \nu_{[-l]}^*, \mu_i^*, V_i^*, \Psi_{[-l]}^*), \quad (2.9)$$

where $\nu_{[-l]}^* = \nu_0 + n_{k,[-l]}$, $n_{k,[-l]}$ is the cardinality of $\mathcal{S}_{k,[-l]}$ (which is the set of locations in $\mathcal{D}_{k,[-l]}$), and $\Psi_{[-l]}^* = \Psi_0 + (\alpha_j^{-1} - 1)Y_{k,[-l]}^T Y_{k,[-l]} + m_0^T M_0 m_0 - \mu_{\gamma,[-l]}^* V_{[-l]}^{-1*} \mu_{\gamma,[-l]}^*$. While $V_i^* = M_{y,i} V_{\gamma}^* M_{y,i}^T + V_{\Omega_i} + (\alpha_j^{-1} - 1)$, $\mu_i^* = M_{y,i} \mu_{\gamma,[-l]}^*$, which are defined by computing the following auxiliary quantities: $V_{\gamma,[-l]}^{-1*} = \begin{bmatrix} \frac{\alpha_j}{1-\alpha_j} X_{k,[-l]}^T X_{k,[-l]} + M_0^{-1} & \frac{\alpha_j}{1-\alpha_j} X_{k,[-l]}^T \\ \frac{\alpha_j}{1-\alpha_j} X_{k,[-l]} & \rho_{\phi_j}^{-1}(\mathcal{S}_{k,[-l]}, \mathcal{S}_{k,[-l]}) + \frac{\alpha_j}{1-\alpha_j} \mathbb{I}_{n_{k,[-l]}} \end{bmatrix}$, $\mu_{\gamma,[-l]}^* = V_{\gamma,[-l]}^* \begin{bmatrix} \frac{\alpha_j}{1-\alpha_j} X_{k,[-l]}^T Y_{k,[-l]} + m_0 \\ \frac{\alpha_j}{1-\alpha_j} Y_{k,[-l]} \end{bmatrix}$, $M_{y,i} = \begin{bmatrix} X_{k,i} & \rho_{\phi_j}(\mathcal{S}_{k,i}, \mathcal{S}_{k,[-l]}) \rho_{\phi_j}^{-1}(\mathcal{S}_{k,[-l]}, \mathcal{S}_{k,[-l]}) \end{bmatrix}$, and $V_{\Omega_i} = \rho_{\phi_j}(\mathcal{S}_{k,i}, \mathcal{S}_{k,i}) - \rho_{\phi_j}(\mathcal{S}_{k,i}, \mathcal{S}_{k,[-l]}) \rho_{\phi_j}^{-1}(\mathcal{S}_{k,[-l]}, \mathcal{S}_{k,[-l]}) \rho_{\phi_j}(\mathcal{S}_{k,[-l]}, \mathcal{S}_{k,i})$. Note that $\nu_{[-l]}^*$ is scalar, μ_i^* is $(1 \times q)$ row vector, V_i^* is a scalar, and $\Psi_{[-l]}^*$ is $(q \times q)$ matrix. Further details, including derivations and implementation, are supplied in Section S2.1 and Algorithm 1.

For each dataset \mathcal{D}_k , BPS computes: (i) an estimate of the posterior predictive $\hat{p}(\cdot ; \mathcal{D}_k) = \sum_{j=1}^J \hat{z}_{k,j} p(\cdot | \mathcal{D}_k, \mathcal{M}_j)$ for $k = 1, \dots, K$ and $j = 1, \dots, J$; and (ii) a set of stacking weights $\hat{z}_k = \{\hat{z}_{k,j}\}_{j=1, \dots, J}$. Once these weights are available, we apply BPS a second time to obtain a weighted average of $\hat{p}(\cdot ; \mathcal{D}_k)$ over the k subsets. This DOUBLE BPS (DBPS) of predictive densities seeks weights $w = \{w_k\}_{k=1, \dots, K}$ such that $\hat{w} = \max_{w \in S_1^K} \frac{1}{n} \sum_{i=1}^n \log \sum_{k=1}^K w_k \hat{p}(Y_i | \mathcal{D}_k)$ (see Section S4.1). Once stacking weights $\hat{w} = \{\hat{w}_k\}_{k=1, \dots, K}$ are computed using Algorithm 2, sampling from the posterior and posterior predictive distributions is obtained from

$$\hat{p}(\cdot ; \mathcal{D}) = \sum_{k=1}^K \hat{w}_k \sum_{j=1}^J \hat{z}_{k,j} p(\cdot | \mathcal{D}_k, \mathcal{M}_j) . \quad (2.10)$$

Only posterior predictive distributions are considered to acquire the two sets of stacking weights. Given the weights obtained from double stacking, the stacked posterior distribution is a mixture of finite mixtures. This makes sampling from (2.10) straightforward.

First, the set of stacking weights $\hat{z}_k = \{\hat{z}_{k,j}\}_{j=1,\dots,J}$ obtained using BPS within the subset of the data \mathcal{D}_k , is primarily used to approximate the subset posterior distribution $\hat{p}(\Theta ; \mathcal{D}_k) = \sum_{j=1}^J \hat{z}_{k,j} p(\Theta | \mathcal{D}_k, \mathcal{M}_j)$, for each subset $k = 1, \dots, K$. By considering the second set of stacking weights $\hat{w} = \{\hat{w}_k\}_{k=1,\dots,K}$, the stacked full posterior distribution is $\hat{p}(\Theta ; \mathcal{D}) = \sum_{k=1}^K \hat{w}_k \hat{p}(\Theta ; \mathcal{D}_k) = \sum_{k=1}^K \hat{w}_k \sum_{j=1}^J \hat{z}_{k,j} p(\Theta | \mathcal{D}_k, \mathcal{M}_j)$, where $\Theta = \{\gamma, \Sigma\}$. This is a substantial simplification over meta-kriging (Guhaniyogi and Banerjee, 2018, 2019) that does not require any empirical approximation of posterior or predictive distributions. Again, the predictive random variable $Y_{\mathcal{U}}$ is recovered from (2.10) as

$$\hat{p}(Y_{\mathcal{U}} ; \mathcal{D}) = \sum_{k=1}^K \hat{w}_k \sum_{j=1}^J \hat{z}_{k,j} p(Y_{\mathcal{U}} | \mathcal{D}_k, \mathcal{M}_j). \quad (2.11)$$

Inferential interest resides with the posterior predictive surface for Ω . Thus, we estimate $\Omega_{\mathcal{U}}$ using $\hat{p}(\Omega_{\mathcal{U}} ; \mathcal{D}) = \sum_{k=1}^K \hat{w}_k \hat{p}(\Omega_{\mathcal{U}} ; \mathcal{D}_k)$, where $\hat{p}(\Omega_{\mathcal{U}} ; \mathcal{D}_k) = \sum_{j=1}^J \hat{z}_{k,j} p(\Omega_{\mathcal{U}} | \mathcal{D}_k, \mathcal{M}_j)$.

3 Computer programs and resources

All our subsequent analysis are implemented in native R and c++ deploying the **spBPS** package. All programs required to reproduce the analysis are publicly accessible from the GitHub repository [lucapresicce/Bayesian-Transfer-Learning-for-GeoAI](https://github.com/lucapresicce/Bayesian-Transfer-Learning-for-GeoAI) that links the Rcpp-based **spBPS** package. The reported results are from a standard laptop running an Intel Core i7-8750H CPU with 5 cores for parallel computation and 16 GB of RAM.

We fit a linear model of coregionalization (LMC, Banerjee et al., 2015) and multivariate seemingly unrelated Bayesian additive regression trees (multivariate BART Esser et al., 2025) using **spBayes** and **subBART** packages, respectively. We also compare with machine learning

Algorithm 1 Computing stacking weights within subsets using BPS

Input: Y ($n \times q$ matrix of outcomes), X ($n \times p$ design matrix), \mathcal{S} (coordinates of n locations); $\{m_0, M_0, \Psi_0, \nu_0\}$: Prior parameters; $G_\alpha \times G_\phi$: Grids of $\{\alpha, \phi\}$; n (no. of locations), q (no. of outcomes), p (no. of predictors); K (no. of subsets), J (no. of models), L (no. of folds).

Output: $\hat{z} = \{\hat{z}_k = \{\hat{z}_{k,j}\} : k = 1, \dots, K, j = 1, \dots, J\}$: Stacking weights within subsets; $\{pd_{k,j,i} : k = 1, \dots, K, j = 1, \dots, J, i = 1, \dots, n\}$: point-wise predictive density of Y ; G_{all} : Grid of dimension J , spanned by G_α, G_ϕ

```

1: Partition  $Y, X, \mathcal{S}$  into  $\mathcal{D}_k = \{Y_k, X_k, \mathcal{S}_k\}$ ,  $k = 1, \dots, K$ 
2: Store  $n_k$ , as cardinality of  $\mathcal{S}_k$ ; Compute  $G_{all}$  by expanding  $G_\alpha, G_\phi$ 
3: for  $k = 1, \dots, K$  do Parallel
4:   for  $j = 1, \dots, J$  do
5:     Extract  $\{\alpha_j, \phi_j\}$  from  $j$ -th row of  $G_{all}$ 
6:     Form  $L$  folds:  $\mathcal{D}_{k,[l]} = \{Y_{k,[l]}, X_{k,[l]}, \mathcal{S}_{k,[l]}\}$  and  $\mathcal{D}_{k,[-l]} = \{Y_{k,[-l]}, X_{k,[-l]}, \mathcal{S}_{k,[-l]}\}$ 
7:     Store  $n_{k,[-l]}$ , as cardinality of  $\mathcal{S}_{k,[-l]}$ 
8:     for  $l = 1, \dots, L$  do
9:       Compute  $R_{\phi_j}([-l]) = \rho_{\phi_j}(\mathcal{S}_{k,[-l]}, \mathcal{S}_{k,[-l]})$ ,  $R_{\phi_j}^{-1}([-l])$  and  $M_0$  for  $M_0^{-1}$ 
10:      Construct  $V_{\gamma,[-l]}^{-1\star} = \begin{bmatrix} \frac{\alpha_j}{1-\alpha_j} X_{k,[-l]}^T X_{k,[-l]} + M_0^{-1} & \frac{\alpha_j}{1-\alpha_j} X_{k,[-l]}^T \\ \frac{\alpha_j}{1-\alpha_j} X_{k,[-l]} & R_{\phi_j}^{-1}([-l]) + \frac{\alpha_j}{1-\alpha_j} \mathbb{I}_{n_{k,[-l]}} \end{bmatrix}$ 
11:      Solve for  $\mu_{\gamma,[-l]}^\star$ :  $V_{\gamma,[-l]}^{-1\star} \mu_{\gamma,[-l]}^\star = \begin{bmatrix} \frac{\alpha_j}{1-\alpha_j} X_{k,[-l]}^T Y_{k,[-l]} + m_0 \\ \frac{\alpha_j}{1-\alpha_j} Y_{k,[-l]} \end{bmatrix}$ 
12:      Calculate  $\Psi_{[-l]}^\star = \Psi_0 + (\alpha_j^{-1} - 1) Y_{k,[-l]}^T Y_{k,[-l]} + m_0^T M_0 m_0 - \mu_{\gamma,[-l]}^{\star T} V_{[-l]}^{-1\star} \mu_{\gamma,[-l]}^\star$ 
13:      Calculate  $\nu_{[-l]}^\star = \nu_0 + n_{k,[-l]}$ 
14:      for  $i \in [l]$  do
15:        Compute  $R_{\phi_j}(i) = \rho_{\phi_j}(\mathcal{S}_{k,i}, \mathcal{S}_{k,i})$  and  $R_{\phi_j}(i, [-l]) = \rho_{\phi_j}(\mathcal{S}_{k,i}, \mathcal{S}_{k,[-l]})$ 
16:        Calculate  $M_i = R_{\phi_j}(i, [-l]) R_{\phi_j}^{-1}([-l])$  and form  $M_{y,i} = [X_{k,i} \quad M_i]$ 
17:        Calculate  $\mu_i^\star = M_{y,i} \mu_{\gamma,[-l]}^\star$  and  $V_{\Omega_i} = R_{\phi_j}(i) - M_i R_{\phi_j}([-l], i)$ 
18:        Construct  $V_{e,i} = V_{\Omega_i} + (\alpha_j^{-1} - 1)$  and  $V_i^\star = M_{y,i} V_{\gamma,[-l]}^\star M_{y,i}^T + V_{e,i}$ 
19:        Compute  $pd_{k,j,i} = T_{1,q}(Y_{k,i} \mid \nu_{[-l]}^\star, \mu_i^\star, V_i^\star, \Psi_{[-l]}^\star)$ .
20:      end for
21:    end for
22:  end for
23:  Solve:  $\max_{z_k \in S_1^J} \frac{1}{n_k} \sum_{i=1}^{n_k} \log \sum_{j=1}^J z_{k,j} pd_{k,j,i}$  such that  $z_k \in [0, 1]^J : \sum_{j=1}^J z_{k,j} = 1$ 
24: end Parallel for
25: return  $\{\hat{z}, \{pd_{k,j,i}\}, G_{all}\}$ 

```

methods and AI systems using a scalable platform for parallelized supervised and unsupervised machine learning algorithms offered by `h2o` (Fryda et al., 2024). We specifically fit distributed random forest (DRF), gradient boosting (GBM), deep neural network (DNN), and a fully automatic machine learning algorithm (AUTOML). For parallel implementations of DBPS, we employ R packages `doParallel`, and `foreach` (Corporation and Weston, 2022; Microsoft and Weston, 2022). We map the interpolated spatial surfaces using `MBA` (Finley et al., 2022), while sampling from the matrix-variate normal and t distributions is achieved using

Algorithm 2 Calculating stacking weights between subsets using BPS

Input: $\hat{z} = \{\hat{z}_k = \{\hat{z}_{k,j}\} : k \in \{1, \dots, K\}, j \in \{1, \dots, J\}\}$: Stacking weights within subsets; $\{pd_{k,j,i} : k = 1, \dots, K, j = 1, \dots, J, i = 1, \dots, n\}$: point-wise predictive density of Y ; n, q, p : Number of rows, number of outcomes, and number of predictors; $K, \{n_k : k \in \{1, \dots, K\}\}, J$: Number of subsets, dimension of each subset, and number of competitive models in each subset.

Output: $\hat{w} = \{\hat{w}_k : k = 1, \dots, K\}$: Stacking weights between subsets.

```
1: Construct  $pd = [pd_1^T : \dots : pd_K^T]^T$  of dimension  $(n \times J)$ 
   where  $pd_k = \begin{bmatrix} pd_{k,1,1} & \dots & pd_{k,J,1} \\ \vdots & pd_{k,j,i} & \vdots \\ pd_{k,1,n_k} & \dots & pd_{k,J,n_k} \end{bmatrix}$  of dimension  $(n_k \times J)$ 
2: for  $k = 1, \dots, K$  do
3:   Compute  $epd_k = pd \hat{z}_k$  of dimension  $(n \times 1)$ 
4: end for
5: Solve convex optimization problem:
    $\max_{w \in S_1^K} \frac{1}{n} \sum_{i=1}^n \log \sum_{k=1}^K w_k epd_{k,i} = \max_{w \in S_1^K} \frac{1}{n} \sum_{i=1}^n \log \sum_{k=1}^K w_k \sum_{j=1}^J \hat{z}_{k,j} pd_{k,j,i}$ 
   where  $pd_{k,j,i} = p(Y_{k,i} | \mathcal{D}_{k,[-l]}, \mathcal{M}_j) = T_{1,q}(Y_{k,i} | \nu_{[-l]}^*, \mu_i^*, V_i^*, \Psi_{[-l]}^*)$ 
   for  $\forall i \notin [-l], l \in \{1, \dots, L\}$  and  $S_1^K = \{w \in [0, 1]^K : \sum_{k=1}^K w_k = 1\}$ 
6: return  $\hat{w} = \{\hat{w}_k : k \in \{1, \dots, K\}\}$ 
```

`mvnfast` (Fasiolo, 2014). Section S4 specifies computational considerations and sensitivity to the number of data shards, K , for spatial “BIG” data analysis.

We build a Bayesian transfer learning engine to conduct amortized Bayesian inference (Zammit-Mangion et al., 2024) using DBPS. We implement a residual neural network (ResNet) (He et al., 2015) using the R interfaces supplied by `tensorflow` (Allaire et al., 2024) and `keras` (Kalinowski et al., 2024) for native Python.

4 Simulation experiments

We evaluate computational and inferential performances of DOUBLE BPS, while underscoring comparisons with multiple alternative methodologies. We present a selection of simulation results for multivariate models here and refer the reader to Section S5 for further experiments.

4.1 Simulation - Transfer learning in \mathcal{M} -closed & \mathcal{M} -open settings

We evaluate inferential and predictive performance under different settings. We explore how DOUBLE BPS behaves in the \mathcal{M} -closed and \mathcal{M} -open settings and compare with an exact

transfer learning framework we devise in Section 2.1. In the latter, model specification is characterized by different values of α and ϕ representing (i) well-specified (ws) setting with the data generating values $\{\alpha = 0.8, \phi = 4\}$; (ii) moderately misspecified (ms) setting with $\{\alpha = 0.45, \phi = 6.63\}$; and (iii) a highly misspecified (hms) setting with $\{\alpha = 0.25, \phi = 50\}$.

The DOUBLE BPS was tested over \mathcal{M} -closed and \mathcal{M} -open settings. The former considers situations where the true model exists, and it is identified within a finite set of considered models. Here, the “true” model is the one such that $\{\alpha = 0.8, \phi = 4\}$. Then, for DOUBLE BPS under closed setting (BPS-C) we specify $J = 9$ competitive models with $\alpha \in \{0.75, 0.80, 0.85\}$ and $\phi \in \{2, 4, 6\}$ that yields effective spatial ranges in the percentage of maximum point inter-distance of 105%, 53%, 35% respectively, including the true model as one of the possible candidates. Conversely, in the \mathcal{M} -closed setting, even though the true model exists, it cannot be fully specified. Thus, for DOUBLE BPS under open setting (BPS-O), we randomly define $J = 9$ candidate models. In particular, we uniformly sample 3 values for $\alpha \in (0, 1)$ and 3 values for $\phi \in (0, 50)$. We perform the experiment using 50 replications. Each replicate consists of values of $n \times q$ outcome Y generated from (2.4) with $n = 5,000$, $q = 3$ and $p = 2$, X includes an intercept and a predictor generated from a standard uniform distribution over $[0, 1]$, $\beta = \begin{bmatrix} -0.75 & 1.05 & -0.35 \\ 2.20 & -1.10 & 0.45 \end{bmatrix}$ and $\Sigma = \begin{bmatrix} 2.00 & 0.80 & 0.20 \\ 0.80 & 2.00 & -0.45 \\ 0.20 & -0.45 & 2.00 \end{bmatrix}$. The $n \times n$ spatial correlation matrix V is specified using an exponential correlation function with $\phi = 4$ and $\alpha = 0.8$.

Figure 2 presents (i) mean square prediction error (MSPE); (ii) predictive interval width; (iii) absolute bias; and (iv) variance. We present boxplots for the distribution of each metric over the 50 replicates. This is made for each response and for each setting. In terms of predictive MSPE, absolute bias, and variance, the settings BPS-C, BPS-O depict slightly better performance. However, this seems to be compromising predictive interval width as the uncertainty of prediction results is much higher. Approaches that estimate $\{\alpha, \phi\}$, rather than fix them, more uncertainty is somehow expected. In addition, we find no evidence of any difference between BPS-C, and BPS-O for any metric. This is surprising, as it suggests

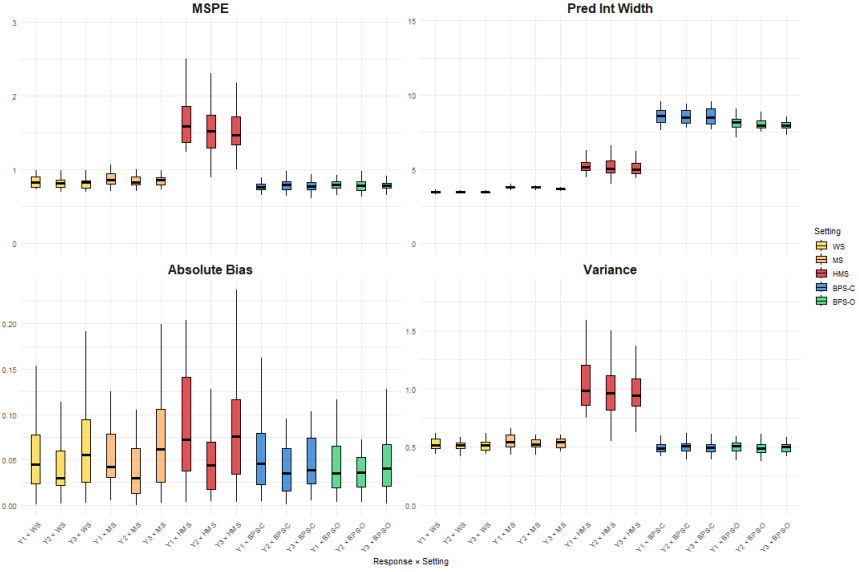


Figure 2: Predictive MSPE, interval width, absolute bias, and variance boxplot across responses and settings from 50 replications.

the reliability of DBPS even under the transfer learning setting we devise in Section 2.3.

Finally, irrespective of \mathcal{M} -closed or \mathcal{M} -open settings, it is more convenient to specify a set of candidate models using DOUBLE BPS instead of attempting to fix $\{\alpha, \phi\}$.

Figure 3 presents posterior inference for (i) average empirical bias; (ii) average coverage; and (iii) average standard deviation, where the average is taken over the 50 replications. As expected, misspecification induces empirical bias in posterior estimates. The top panel reports how greater levels of bias are associated with models that are farther away from the truth. Here, DOUBLE BPS is placed in the middle for both \mathcal{M} settings. The middle plot in Figure 3 shows that Σ is the most affected parameter by misspecifications. Its elements are well captured only by DOUBLE BPS, with coverage close to nominal, followed by ws specification, which performs worse. A Similar pattern holds for β , where only DOUBLE BPS ensures adequate coverage. This reflects greater posterior variability in stacking approaches, as shown in the bottom panel reporting posterior standard deviations across settings. Unsurprisingly, inferential performance is weakest for the spatial variance, which is not identifiable from the realized data (Zhang, 2004). DOUBLE BPS behaves very similarly among \mathcal{M} -closed and \mathcal{M} -open. Additional simulation experiments are discussed in Section S5.



Figure 3: Average posterior bias, coverage, and standard deviation across parameters and settings from 50 replications.

While DBPS outperforms exact transfer learning (Section 2) in \mathcal{M} -closed and \mathcal{M} -open settings, the latter performs competitively with improved predictive performance in WS and MS settings than with HMS. Our overall findings appear consistent with theoretical insights that Gaussian processes tend to deliver good predictive performance even for misspecified covariance functions in fixed domains (Stein, 1988; Stein and Handcock, 1989).

4.2 Amortized Bayesian inference

We conduct transfer learning by supervising a neural network using the outputs of DOUBLE BPS to deliver amortized Bayesian inference. We generate 100 instances of Y from (2.4) using a fixed realization of Ω for $q = 2$ correlated outcomes, $n = 500$ spatial locations that remain fixed across the datasets, and a fixed design matrix X with $p = 2$ comprising an intercept and a single predictor whose values were sampled independently from a uniform distribution over $[0, 1]$. The true regression coefficients are fixed at $\beta = \begin{bmatrix} -0.75 & 1.85 \\ 0.9 & -1.10 \end{bmatrix}$, with $\Sigma = \begin{bmatrix} 1 & -0.3 \\ -0.3 & 1 \end{bmatrix}$, $\alpha = 0.8$, and $\rho_\phi(s_i, s_j) = \exp(-\phi \|s_i - s_j\|)$ with $\phi = 4$.

We train the neural network using $R = 250$ posterior samples by applying DOUBLE BPS to each generated dataset with $K = 5$ subsets, $\alpha \in \{0.7, 0.8, 0.9\}$ and $\phi \in \{3, 4, 5\}$. These

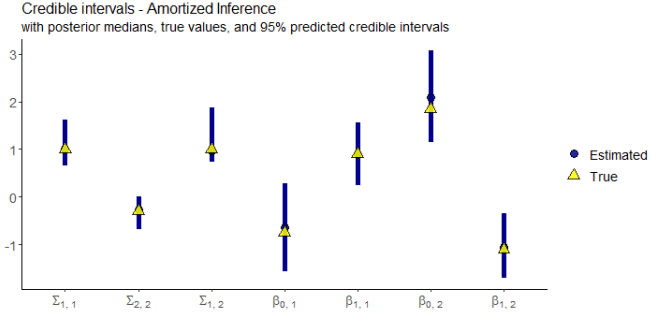


Figure 4: Amortized posterior credible intervals for parameters. True parameters in yellow.

yield 100 instances of $\{Z, \Theta\}$, where $Z = [Y : X] \in \mathbb{R}^{n \times (q+p)}$ and $\Theta \in \mathbb{R}^{[(qp)+(q(q+1)/2)+(nq)] \times 3}$ comprises the $\{2.5, 50, 97.5\}$ posterior quantiles for the distinct elements of $\{\beta, \Sigma, \Omega\}$.

We use a deep neural network comprising 3 hidden layers with 128, 256, and 512 nodes, with ReLU activations. The residual network is trained over 50 epochs with 24 batches per epoch. For evaluation, we apply the trained model to unseen datasets with the same dimensions. Figure 4 displays the predicted posterior intervals (blue bars) for $\{\beta, \Sigma\}$, along with the true values of the parameters (yellow triangles). The credible intervals 95% capture all true values and the predicted medians (50%) align closely with the true values, highlighting the strong predictive precision of the deep network in recovering posterior summaries. Figure 5 displays the predicted posteriors for Ω quantiles. We compare the results from amortized inference, with the true Ω , and the DOUBLE BPS prediction for 50th quantile, presented in the first and the second column of Figure 5, respectively.

These results illustrate the strengths of amortized inference and transfer learning. Once trained, the deep network provides instant posterior quantile estimates for new datasets, without requiring us to rerun DOUBLE BPS. This amortizes the computational cost for future tasks. Additionally, the model generalizes across a range of data-generating conditions effectively enabling posterior transfer learning to new but structurally similar problems. This makes the approach especially useful in large-scale or resource-constrained applications where repeated full Bayesian inference is prohibitively expensive.

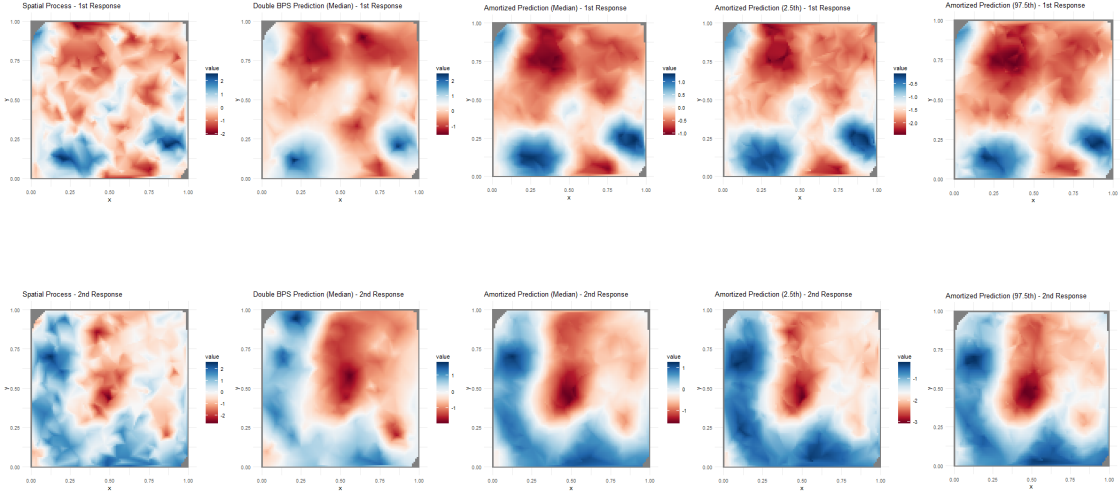


Figure 5: Surface interpolations for true spatial process, BPS prediction (50 quantile), and Amortized prediction of $\{50, 2.5, 97.5\}$ quantiles. Each row corresponds to an outcome.

5 Data analysis

5.1 Vegetation index data

Statisticians and scientists face growing demands to analyze and study global warming datasets (see, e.g., [Fisher, 1958](#); [Nicholls, 1989](#); [Friehe et al., 1991](#); [O’Carroll et al., 2019](#)).

The sheer volume of such datasets and the process-driven models required for their analysis have naturally raised the question of migrating such analysis to AI platforms. Our current application analyzes vegetation index data from the Moderate Resolution Imaging Spectroradiometer (MODIS) developed by NASA. We specifically focus on “MOD13C1.061 - Terra Vegetation Indices 16-Day L3 Global 0.05 Deg Climate Modeling Grid” ([Didan, 2021](#)), which provides vegetation indices per pixel on a 0.05-degree climate modeling grid (3600 rows by 7200 columns of 5600-meter pixels). It contains 16-day global composites, cloud-contamination-free, with additional reflectance and angular information.

Modeling Normalized Difference Vegetation Index (NDVI) and Red Reflection (RR) jointly is scientifically important because it separates and defines the specific biophysical factors influencing vegetation. NDVI is built on the fundamental principle that healthy vegetation absorbs red light and reflects near-infrared (NIR) light. By examining both the calculated

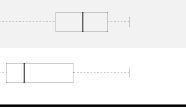
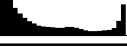
Vegetation index	Mean	Std.Dev	Min.	Max.	Histogram	Boxplot
NDVI	8.593	0.517	6.909	9.469		
Red Reflectance	8.563	0.447	8.007	9.472		

Table 1: Summary statistics and visual representation of response variables.

NDVI and its red reflectance component, scientists can gain deeper insights into vegetation’s structural and biochemical properties. The solar zenith angle (sza), which is the angle between the Sun and the point directly overhead, is a shared predictor that influences how much solar irradiation reaches the surface and is, therefore, crucial when assessing biomass and vegetation indices. NDVI and RR reflect the ability of vegetation to absorb photosynthetically active radiation and help scientists understand processes underlying climate change (Tucker, 1979; Sellers, 1985; Justice et al., 1985; Haque et al., 2024).

The dataset comprises 1,500,000 locations. We randomly selected 1,002,500 sites, reserving 2,500 for predictive evaluation. Following Zhang and Banerjee (2022), outcomes were log-transformed and we labeled $\log(\text{NDVI} + 1)$ as NDVI and $\log(\text{RR} + 1)$ as RR. All variables, including sza, were averaged over a 16-day window in May 2024. Table 1 summarizes the spatial responses distribution. The maximum inter-site distance among sites is approximately 42,909 kilometers.

Our central scientific objective is to jointly predict NDVI and RR from massive, globally distributed datasets of this scale using GEOAI. We assess whether multivariate statistical models can deliver accurate, scalable, and timely predictions across millions of spatial locations while accounting for dependence structures in the solar zenith angle. These capabilities are crucial for application in ecology, agriculture, and climate policy.

5.2 Results using DBPS

To analyze our Vegetation Index (vi) data, we follow machine-generated exploratory data analysis (EDA) described in Section S1. The predictors comprise an intercept and the solar

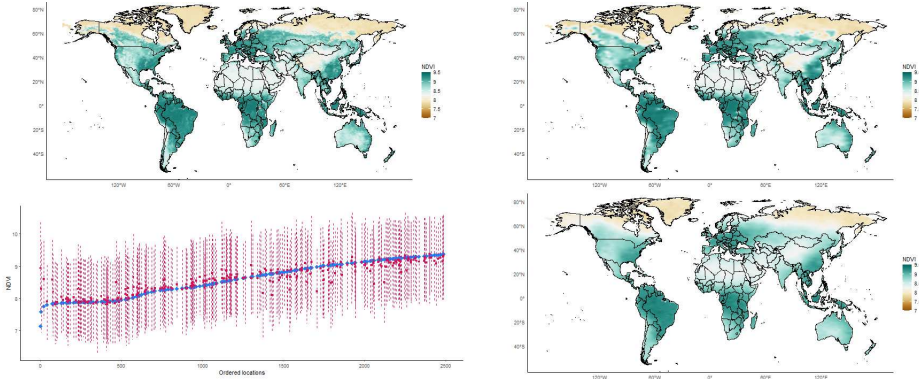


Figure 6: Left to right: Maps for training data (top left), test data (top right) and predicted surface (bottom right) for NDVI. Empirical coverage for held-out values are in the bottom left. Results correspond to $K = 2,000$.

zenith angle for that location ($p = 2$). Based on Section S1, we set $\alpha \in \{0.825, 0.909\}$, and $\phi \in \{0.049, 0.067\}$ respectively. We specify $\{\gamma, \Sigma\}$ in (2.5) using $m_0 = 0_{p \times q}$, $M_0 = 10\mathbb{I}_p$, $\Psi_0 = \mathbb{I}_q$, $\nu_0 = 3$, and finally we opt for an exponential spatial covariance function. Following insights from Section S5.2, we fix the subset size at $n_k \in \{250, 500\}$, leading to a number of subsets $K \in \{4,000, 2,000\}$ respectively. We use a random scheme to form the partition of the dataset and present results when $K = 2,000$ and in Table 2 for $K = 4,000$.

The multivariate model developed in Section 2.3 with NDVI and RR comprising the $q = 2$ columns of Y . Figures 6 and 7 illustrate maps corresponding to NDVI and RR, respectively, using $K = 2,000$ subsets. The top left panel in each figure presents the spatially interpolated map of the training data for the respective responses. The interpolated maps for the test data are displayed in the top right panel of the respective figures. These maps reveal pronounced spatial variation, where the darker shades of green in NDVI represent higher values of detected biomass, while lighter shades of brown represent low biomass. Conversely for RR, warmer colors in the red spectrum represent higher reflectance.

Figures 6 and 7 show results from DOUBLE BPS. Maps of interpolated posterior means and predicted responses are displayed in the bottom right of the respective figures. The DBPS interpolated maps are almost indistinguishable from the true surface (top right). This suggests that the automated DBPS effectively, perhaps even strikingly, recovers the spatial patterns in spite of the modeling simplifications over more elaborate statistical models

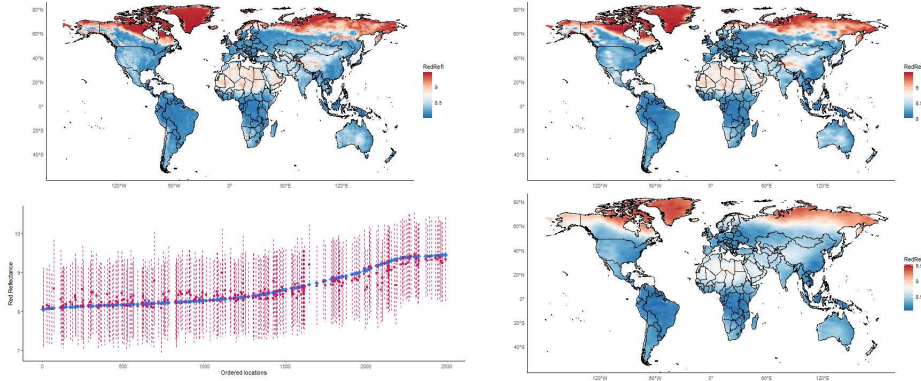


Figure 7: Left to right: Maps for training data (top left), test data (top right) and predicted surface (bottom right) for RR. Empirical coverage for held-out values of outcomes (bottom left). Results correspond to $K = 2,000$.

Parameter	Conjugate Linear model	DBPS ($K = 4,000$)	DBPS ($K = 2,000$)
$\beta_{0, \text{NDVI}}$	34.495 (34.392, 34.601)	1.364 (-1.039, 3.907)	1.767 (-0.422, 3.917)
$\beta_{1, \text{NDVI}}$	-2.708 (-2.719, -2.697)	0.744 (0.478, 0.998)	0.707 (0.485, 0.939)
$\beta_{0, \text{RR}}$	-16.924 (-17.014, -16.837)	-0.418 (-2.470, 1.710)	-0.562 (-2.187, 0.962)
$\beta_{1, \text{RR}}$	2.664 (2.655, 2.674)	0.945 (0.726, 1.158)	0.959 (0.795, 1.139)
Σ_{NDVI}	0.221 (0.220, 0.221)	0.182 (0.130, 0.257)	0.119 (0.099, 0.146)
$\Sigma_{\text{NDVI, RR}}$	-0.167 (-0.168, -0.166)	-0.114 (-0.173, -0.079)	-0.076 (-0.094, -0.061)
Σ_{RR}	0.155 (0.154, 0.155)	0.115 (0.082, 0.170)	0.077 (0.062, 0.092)

Table 2: Vegetation Index data analysis parameter estimates for candidate models. Parameter posterior summary 50 (2.5, 97.5) percentiles.

(Banerjee, 2020; Zhang et al., 2021). The predictive 95% credible intervals when $K = 2,000$ for both responses are shown in the bottom left of Figures 6 and 7, respectively.

Table 2 compares model parameters posterior estimates for DBPS with $K \in \{4,000, 2,000\}$, and the Bayesian conjugate linear model, which does not take into account spatial variability. The notably higher magnitudes of the intercepts in the non-spatial linear model are unsurprising as the spatial random effects absorb much of the variation in the intercepts. The solar zenith angle is positively associated with RR and negatively associated with NDVI in the non-spatial model. This, too, is expected since higher levels of solar irradiation are associated with higher red reflectance and with more arid regions with less vegetation. However, the spatial models reveal that the slope for NDVI is significantly positive with solar irradiation after the spatial effects have absorbed previously unaccounted latent or lurking factors that might have contributed to the negative slopes in the non-spatial model.

In addition to DOUBLE BPS (DBPS) and Bayesian multivariate linear regression, we expanded the analysis by including four competitive algorithms: distributed random forest (DRF), gradient boosting (GBM), deep neural network (DNN), and a fully automatic machine

Model	Time (min)	RMSPE	$\rho_{\text{NDVI,RR}}$
DBPS ($K = 2,000$)	81	[0.206, 0.159, 0.183]	-0.844 (-0.880, -0.795)
DBPS ($K = 4,000$)	21	[0.241, 0.197, 0.219]	-0.816 (-0.874, -0.706)
Conjugate Linear Model	12	[0.474, 0.404, 0.439]	-0.921 (-0.928, -0.915)
GBM	2	[0.419, 0.352, 0.385]	-0.993 (-,-)
DRF	10	[0.420, 0.353, 0.386]	-0.991 (-,-)
DNN	26	[0.422, 0.354, 0.388]	-0.987 (-,-)
AUTOML	44	[0.419, 0.352, 0.385]	-0.993 (-,-)

Table 3: Vegetation Index data analysis computing time in minutes, RMSPE, and empirical correlation (ρ) for candidate models. Root mean square prediction error(s) presentation [NDVI, red reflectance, average].

learning algorithm (AUTOML). As detailed in Section S4, we implement and perform the analysis using the `h2o` R package (Fryda et al., 2024). As no method for multivariate models is available within the `h2o` framework, we fit these algorithms separately for NDVI, and RR, considering the same explanatory variables. Then, we compute the empirical correlation among the predictions. In Table 3, we offer a comparison of computational costs, predictive performances, and empirical correlation. The DOUBLE BPS dominates both running time and predictive performances. It achieves an RMSPE of (0.206, 0.159) when $K = 2,000$, and (0.241, 0.197) with $K = 4,000$ subsets for NDVI and RR respectively. This is significantly lower (by almost 100%) than the standard Bayesian conjugate multivariate linear model, which produces RMSPE of (0.474, 0.439) for the two vegetation indexes, respectively. Actually, the DOUBLE BPS outperformed all the other competitive algorithms in terms of RMSPE. This is attained at a fraction of the computational time for other methods, let alone DOUBLE BPS models multivariate distributions jointly, and offer full explainability. Estimates of ρ_{NDVI} and ρ_{RR} reveal a well-documented negative association between the two responses. Indeed, the spatial patterns in these indices are almost the reverse of each other as revealed in Figures 6 and 7. The conjugate Bayesian linear model estimates higher negative correlation, while DBPS tends to underestimate it, considerably so as n_k decreases. We attempted comparisons with the LMC and BART models, but omitted due they exceeded memory.

Recalling that all the analyses are produced on a personal laptop (with just 5 physical cores) with minimal human intervention, the total run time of only 21 minutes with $K = 4,000$ and 81 minutes with $K = 2,000$ for DOUBLE BPS are impressive and confirm the

quadratic dependence of the partition size discussed in Section S5.2. Moreover, the strong dependence on the number of J competitive models assessed is worth noting. Here $J = 4$, this suggests a marginal computational burden for each competitive model.

6 Discussion

This manuscript devises a statistical modeling component for an artificially intelligent geospatial system (GEOAI) tailored to analyze massive data with minimal human intervention. The contribution harnesses analytically accessible multivariate statistical distributions in conjunction with Bayesian predictive stacking to deliver rapid inference by circumventing iterative algorithms that require, often extensive, human tuning. Our proposed GeoSpatial AI system relies on Bayesian transfer learning using double Bayesian predictive stacking to process massive amounts of streaming spatial data on high-performance CPU architectures.

Some additional remarks are warranted. The development here has been elucidated with a hierarchical matrix-variate spatial process framework. Although modeling simplifications have been introduced to minimize human intervention, we emphasize that DBPS seamlessly applies to more versatile but analytically intractable models. For spatially misaligned multivariate data, where not all variables have been observed in the same set of locations, we encounter missing entries in Y using analytically tractable closed-form distribution theory (Zhang and Banerjee, 2022). Should users wish to explore more complex models with unknown $\{\alpha, \phi\}$ or work with alternate multivariate models, we can implement Bayesian inference (using MCMC, Variational Bayes or Laplace approximations) on each subset and invoke BPS to pool across the subsets of the data. The time for analyzing each subset increases due to model complexity, but scaling inference to massive datasets is still achieved by BPS—and this too with considerable efficiency over divide-and-conquer approaches such as the geometric median, or GM, of posteriors (see meta-kriging in Guhaniyogi and Banerjee, 2018).

Future research can build upon recent work by [Cabel et al. \(2025\)](#) to enrich spatial-temporal dependence structures within DBPS and to further accelerate amortized inference.

Section [2.3](#) devised posterior inference as a “mixture of mixtures”. Following [Yao et al. \(2018\)](#), we prefer stacking to fitting a mixture model because the former is numerically robust and requires almost no human tuning. Moreover, the structure of mixture-of-mixtures conceptually resembles the “Mixture of Experts” (MOE) that are adopted by AI platforms such as GPT-4 and Mistral. Disseminating our proposed product with our accompanying software, which is currently being migrated to R, is expected to significantly boost GEOSPATIAL AI systems. Future directions will also explore perceived potential of DBPS as a feeder for emerging amortized inference methods ([Ganguly et al., 2023](#); [Zammit-Mangion et al., 2024](#); [Sainsbury-Dale et al., 2024](#)) to achieve Bayesian inference. Rapid delivery of posterior estimates of the entire spatial process from DBPS will amount to more training data for amortized neural learners that can result in accelerated tuning for subsequent Bayesian inference. We do not see our proposed approach as a competitor to, but rather as supplementary to amortized neural inference. Refer to Section [4.2](#) for an effective representation. Such developments will be pursued as future research. We also seek to expand and fully investigate automated DOUBLE BPS using Markovian graphical structures across data subsets to further expedite and improve GEOSPATIAL AI systems.

Supplementary Materials

The online supplement includes exploratory data analyses, and automated settings for model hyperparameters without human intervention (Section [S1](#)), additional derivations and details on matrix-variate distributions (Section [S2](#)), some theoretical insights (Section [S3](#)), computational details and algorithms (Section [S4](#)), and additional simulation experiment results (Section [S5](#)). Computer programs to reproduce all our analysis are publicly accessible from the GitHub repository [lucapresicce/Bayesian-Transfer-Learning-for-GEOAI](https://github.com/lucapresicce/Bayesian-Transfer-Learning-for-GEOAI)

References

Allaire, J. J., Kalinowski, T., Falbel, D., Eddelbuettel, D., Tang, G. I. E., , Posit, and PBC (2024). tensorflow: R Interface to 'TensorFlow'.

Banerjee, S. (2017). High-dimensional Bayesian geostatistics. *Bayesian Analysis*, 12(2):583–614.

Banerjee, S. (2020). Modeling massive spatial datasets using a conjugate Bayesian linear modeling framework. *Spatial Statistics*, 37:100417.

Banerjee, S. (2022). Discussion of “Measuring housing vitality from multi-source big data and machine learning”. *Journal of the American Statistical Association*, 117(539):1063–1065.

Banerjee, S., Carlin, B. P., and Gelfand, A. E. (2015). *Hierarchical modeling and analysis for Spatial Data*. Chapman & Hall/CRC.

Banerjee, S., Gelfand, A. E., Finley, A. O., and Sang, H. (2008). Gaussian predictive process models for large spatial data sets. *Journal of the Royal Statistical Society: Series B (Statistical Methodology)*, 70(4):825–848.

Bell, M. L., Dominici, F., and Samet, J. M. (2005). A meta-analysis of time-series studies of ozone and mortality with comparison to the national morbidity, mortality, and air pollution study. *Epidemiology*, 16(4):436–45.

Breiman, L. (1996). Stacked regressions. *Machine Learning*, 24(1):49–64.

Cabel, D., Sugasawa, S., Kato, M., Takanashi, K., and McAlinn, K. (2025). Bayesian Spatial Predictive Synthesis. arXiv:2203.05197.

Cao, J., Kang, M., Jimenez, F., Sang, H., Schaefer, F. T., and Katzfuss, M. (2023). Variational sparse inverse cholesky approximation for latent Gaussian processes via double

kullback-leibler minimization. volume 202 of *Proceedings of Machine Learning Research*, pages 3559–3576.

Corporation, M. and Weston, S. (2022). *doParallel: Foreach parallel adaptor for the 'parallel' Package*. R package version 1.0.17.

Cressie, N. (1993). *Statistics For Spatial Data, Revised Edition*. John Wiley & Sons.

Cressie, N. and Johannesson, G. (2008). Fixed rank kriging for very large spatial data sets. *Journal of the Royal Statistical Society: Series B (Statistical Methodology)*, 70(1):209–226.

Cressie, N. and Wikle, C. K. (2011). *Statistics for spatio-temporal data*. Wiley.

Datta, A., Banerjee, S., Finley, A. O., and Gelfand, A. E. (2016). Hierarchical nearest-neighbor Gaussian process models for large geostatistical datasets. *Journal of the American Statistical Association*, 111(514):800–812.

Deisenroth, M. and Ng, J. W. (2015). Distributed Gaussian Processes. volume 37 of *Proceedings of International Conference on Machine Learning*, pages 1481–1490.

Dey, D., Datta, A., and Banerjee, S. (2022). Graphical Gaussian process models for highly multivariate spatial data. *Biometrika*, 109(4):993–1014.

Didan, K. (2021). MODIS/Terra Vegetation Indices 16-Day L3 Global 0.05Deg CMG V061 | NASA Earthdata.

Esser, J., Maia, M., Parnell, A. C., Bosmans, J., Dongen, H. v., Klausch, T., and Murphy, K. (2025). Seemingly unrelated Bayesian additive regression trees for cost-effectiveness analyses in healthcare. arXiv:2404.02228.

Fasiolo, M. (2014). *An introduction to mvnfast*. University of Bristol. R package version 0.2.8.

Finley, A., Banerjee, S., and Øyvind Hjelle (2022). *MBA: Multilevel B-spline approximation*.

R package version 0.1-0.

Finley, A. O., Datta, A., Cook, B. D., Morton, D. C., Andersen, H.-E., and Banerjee, S. (2019). Efficient algorithms for Bayesian nearest neighbor Gaussian processes. *Journal of Computational and Graphical Statistics*, 28(2):401–414.

Fisher, E. L. (1958). Hurricanes and the sea-surface temperature field. *Journal of Atmospheric Sciences*, 15(3):328–333.

Friehe, C. A., Shaw, W. J., Rogers, D. P., Davidson, K. L., Large, W. G., Stage, S. A., Crescenti, G. H., Khalsa, S. J. S., Greenhut, G. K., and Li, F. (1991). Air-sea fluxes and surface layer turbulence around a sea surface temperature front. *Journal of Geophysical Research: Oceans*, 96(C5):8593–8609.

Fryda, T., LeDell, E., Gill, N., Aiello, S., Fu, A., Candel, A., Click, C., Kraljevic, T., Nykodym, T., Aboyoun, P., Kurka, M., Malohlava, M., Poirier, S., and Wong, W. (2024). *h2o: R Interface for the 'H2O' Scalable Machine Learning Platform*. R package version 3.44.0.3.

Fu, A., Narasimhan, B., and Boyd, S. (2020). CVXR: An R package for disciplined convex optimization. *Journal of Statistical Software*, 94(14):1–34.

Ganguly, A., Jain, S., and Watchareeruetai, U. (2023). Amortized variational inference: A systematic review. *Journal of Artificial Intelligence Research*, 78:167–215.

Gelfand, A. E., Diggle, P., Guttorp, P., and Fuentes, M. (2010). *Handbook of Spatial Statistics*. Taylor & Francis.

Georganos, S., Grippa, T., Gadiaga, A. N., Linard, C., Lennert, M., Vanhuyse, S., Mboga, N., Wolff, E., and Kalogirou, S. (2021). Geographical random forests: a spatial extension

of the random forest algorithm to address spatial heterogeneity in remote sensing and population modelling. *Geocarto International*, 36(2):121–136.

Gneiting, T. and Raftery, A. E. (2007). Strictly proper scoring rules, prediction, and estimation. *Journal of the American Statistical Association*, 102(477):359–378.

Grant, M. and Boyd, S. (2008). Graph implementations for nonsmooth convex programs. In *Recent Advances in Learning and Control*, pages 95–110. Springer-Verlag Limited.

Guhaniyogi, R. and Banerjee, S. (2018). Meta-kriging: Scalable Bayesian modeling and inference for massive spatial datasets. *Technometrics*, 60(4):430–444.

Guhaniyogi, R. and Banerjee, S. (2019). Multivariate spatial meta kriging. *Statistics & Probability Letters*, 144:3–8.

Guhaniyogi, R., Li, C., Savitsky, T., and Srivastava, S. (2023). Distributed Bayesian Inference in Massive Spatial Data. *Statistical Science*, 38(2):262–284.

Guhaniyogi, R., Li, C., Savitsky, T. D., and Srivastava, S. (2019). A divide-and-conquer Bayesian approach to large-scale kriging. *arXiv preprint*, page arXiv:1712.09767.

Guhaniyogi, R., Li, C., Savitsky, T. D., and Srivastava, S. (2022). Distributed Bayesian Varying Coefficient Modeling Using a Gaussian Process Prior. *Journal of Machine Learning Research*, 23(84):1–59.

Haque, M. A., Reza, M. N., Ali, M., Karim, M. R., Ahmed, S., Lee, K.-D., Khang, Y. H., and Chung, S.-O. (2024). Effects of Environmental Conditions on Vegetation Indices from Multispectral Images: A Review. *Korean Journal of Remote Sensing*, 40(4):319–341. Publisher: Korean Society of Remote Sensing.

He, K., Zhang, X., Ren, S., and Sun, J. (2015). Deep Residual Learning for Image Recognition. *arXiv:1512.03385*.

Heaton, M. J., Datta, A., Finley, A. O., Furrer, R., Guinness, J., Guhaniyogi, R., Gerber, F., Gramacy, R. B., Hammerling, D. M., Katzfuss, M., Lindgren, F., Nychka, D. W., Sun, F., and Zammit-Mangion, A. (2017). A case study competition among methods for analyzing large spatial data. *Journal of Agricultural, Biological, and Environmental Statistics*, 24(3):398–425.

Justice, C. O., Townshend, J. R. G., Holben, B. N., and Tucker, C. J. (1985). Analysis of the phenology of global vegetation using meteorological satellite data. *International Journal of Remote Sensing*, 6(8).

Kalinowski, T., Falbel, D., Allaire, J. J., Chollet, F., RStudio, Google, Tang [ctb, Y., cph, Bijl, W. V. D., Studer, M., and Keydana, S. (2024). keras: R Interface to 'Keras'.

Kang, J., Johnson, T. D., Nichols, T. E., and Wager, T. D. (2011). Meta analysis of functional neuroimaging data via Bayesian spatial point processes. *Journal of the American Statistical Association*, 106(493):124–134.

Katzfuss, M. (2017). A multi-resolution approximation for massive spatial datasets. *Journal of the American Statistical Association*, 112(517):201–214.

Katzfuss, M. and Guinness, J. (2021). A general framework for Vecchia approximations of Gaussian processes. *Statistical Science*, 36(1):124–141.

Lindgren, F., Rue, H., and Lindström, J. (2011). An explicit link between Gaussian fields and Gaussian Markov random fields: The stochastic partial differential equation approach. *Journal of the Royal Statistical Society Series B: Statistical Methodology*, 73(4):423–498.

McAlinn, K., , Knut Are, A., , Jouchi, N., , and West, M. (2020). Multivariate Bayesian Predictive Synthesis in Macroeconomic Forecasting. *Journal of the American Statistical Association*, 115(531):1092–1110.

McAlinn, K. and West, M. (2019). Dynamic Bayesian predictive synthesis in time series forecasting. *Journal of Econometrics*, 210(1):155–169.

Microsoft and Weston, S. (2022). *Foreach: Provides foreach looping construct*. R package version 1.5.2.

Minsker, S., Srivastava, S., Lin, L., and Dunson, D. B. (2017). Robust and scalable Bayes via a median of subset posterior measures. *Journal of Machine Learning Research*, 18(124):1–40.

Nicholls, N. (1989). Sea surface temperatures and australian winter rainfall. *Journal of Climate*, 2(9):965–973.

Nychka, D., Bandyopadhyay, S., Hammerling, D., Lindgren, F., and Sain, S. (2015). A multiresolution gaussian process model for the analysis of large spatial datasets. *Journal of Computational and Graphical Statistics*, 24(2):579–599.

O’Carroll, A. G., Armstrong, E. M., Beggs, H. M., Bouali, M., Casey, K. S., Corlett, G. K., Dash, P., Donlon, C. J., Gentemann, C. L., Høyer, J. L., Ignatov, A., Kabobah, K., Kachi, M., Kurihara, Y., Karagali, I., Maturi, E., Merchant, C. J., Marullo, S., Minnett, P. J., Pennybacker, M., Ramakrishnan, B., Ramsankaran, R., Santoleri, R., Sunder, S., Saux Picart, S., Vázquez-Cuervo, J., and Wimmer, W. (2019). Observational needs of sea surface temperature. *Frontiers in Marine Science*, 6(420):1–27.

Parmigiani, G. (2002). *Modeling in Medical Decision Making: A Bayesian Approach*. John Wiley & Sons, Hoboken, NJ.

Quiñonero-Candela, J. and Rasmussen, C. E. (2005). A unifying view of sparse approximate gaussian process regression. *Journal of Machine Learning Research*, 6(65):1939–1959.

Ren, Q., Banerjee, S., Finley, A. O., and Hodges, J. S. (2011). Variational bayesian methods for spatial data analysis. *Computational Statistics & Data Analysis*, 55(12):3197–3217.

Rendell, L. J., Adam M. Johansen, A. L., and Whiteley, N. (2021). Global consensus Monte Carlo. *Journal of Computational and Graphical Statistics*, 30(2):249–259.

Rue, H., Martino, S., and Chopin, N. (2009). Approximate Bayesian inference for latent Gaussian models by using integrated nested Laplace approximations. *Journal of the Royal Statistical Society Series B: Statistical Methodology*, 71(2):319–392.

Saha, A., Basu, S., and Datta, A. (2023). Random forests for spatially dependent data. *Journal of the American Statistical Association*, 118(541):665–683.

Sainsbury-Dale, M., Zammit-Mangion, A., Richards, J., and Huser, R. (2024). Neural bayes estimators for irregular spatial data using graph neural networks. arXiv:2310.02600.

Sauer, A., Cooper, A., and Gramacy, R. B. (2023a). Vecchia-approximated deep gaussian processes for computer experiments. *Journal of Computational and Graphical Statistics*, 32(3):824–837.

Sauer, A., Gramacy, R. B., and Higdon, D. (2023b). Active learning for deep gaussian process surrogates. *Technometrics*, 65(1):4–18.

Scott, S. L., Alexander W. Blocker, F. V. B., Chipman, H. A., George, E. I., and McCulloch, R. E. (2016). Bayes and big data: the consensus Monte Carlo algorithm. *International Journal of Management Science and Engineering Management*, 11(2):78–88.

Sellers, P. J. (1985). Canopy reflectance, photosynthesis and transpiration. *International Journal of Remote Sensing*, 6(8).

Srivastava, S., Cevher, V., Dinh, Q., and Dunson, D. (2015). WASP: Scalable Bayes via barycenters of subset posteriors. volume 38 of *Proceedings of Machine Learning Research*, pages 912–920.

Srivastava, S., Li, C., and Dunson, D. B. (2018). Scalable Bayes via Barycenter in Wasserstein Space. *Journal of Machine Learning Research*, 19(8):1–35.

Stein, M. L. (1988). Asymptotically efficient prediction of a random field with a misspecified covariance function. *The Annals of Statistics*, 16(1):55–63.

Stein, M. L. (1999). *Interpolation of spatial data*. Springer Series in Statistics. Springer-Verlag, New York. Some theory for Kriging.

Stein, M. L. and Handcock, M. S. (1989). Some asymptotic properties of kriging when the covariance function is misspecified. *Mathematical Geology*, 21:171–190.

Suder, P. M., Xu, J., and Dunson, D. B. (2023). Bayesian Transfer Learning. arXiv:2312.13484.

Talebi, H., Peeters, L. J. M., Otto, A., and Tolosana-Delgado, R. (2022). A truly spatial random forests algorithm for geoscience data analysis and modelling. *Mathematical Geosciences*, 54(1):1–22.

Tallman, E. and West, M. (2023). Bayesian predictive decision synthesis. *Journal of the Royal Statistical Society Series B: Statistical Methodology*, 86(2):340–363.

Tang, W., Zhang, L., and Banerjee, S. (2021). On identifiability and consistency of the nugget in Gaussian spatial process models. *Journal of the Royal Statistical Society: Series B (Statistical Methodology)*, 83(5):1044–1070.

Tucker, C. J. (1979). Red and photographic infrared linear combinations for monitoring vegetation. *Remote Sensing of Environment*, 8(2):127–150.

Vecchia, A. V. (1988). Estimation and model identification for continuous spatial processes. *Journal of the Royal Statistical society, Series B*, 50:297–312.

Wikle, C. K. (2010). Low-rank representations for spatial processes. *Handbook of Spatial Statistics*, pages 107–118.

Wikle, C. K. and Zammit-Mangion, A. (2023). Statistical deep learning for spatial and spatiotemporal data. *Annual Review of Statistics and Its Application*, 10:247–270.

Wolpert, D. H. (1992). Stacked generalization. *Neural Networks*, 5(2):241–259.

Wu, L., Pleiss, G., and Cunningham, J. P. (2022). Variational nearest neighbor Gaussian process. volume 162 of *Proceedings of Machine Learning Research*, pages 24114–24130.

Yao, Y., Vehtari, A., Simpson, D., and Gelman, A. (2018). Using stacking to average Bayesian predictive distributions (with discussion). *Bayesian Analysis*, 13(3):917–1007.

Zammit-Mangion, A., Ng, T. L. J., Vu, Q., and Filippone, M. (2022). Deep compositional spatial models. *Journal of the American Statistical Association*, 117(540):1787–1808.

Zammit-Mangion, A., Sainsbury-Dale, M., and Huser, R. (2024). Neural methods for amortised inference. arXiv:2404.12484.

Zhang, H. (2004). Inconsistent estimation and asymptotically equal interpolations in model-based geostatistics. *Journal of the American Statistical Association*, 99(465):250–261.

Zhang, L. and Banerjee, S. (2022). Spatial factor modeling: A Bayesian matrix-normal approach for misaligned data. *Biometrics*, 78(2):560–573.

Zhang, L., Banerjee, S., and Finley, A. O. (2021). High-dimensional multivariate geostatistics: A Bayesian matrix-normal approach. *Environmetrics*, 32(4):e2675.

Zhou, Y., Xue, L., Shi, Z., Wu, L., and Fan, J. (2022). Measuring housing vitality from multi-source big data and machine learning. *Journal of the American Statistical Association*, 117(539):1045–1059.

Supplemental material: Bayesian Transfer Learning for Artificially Intelligent Geospatial Systems: A Predictive Stacking Approach

Organization of the supplemental material

The supplementary material is organized as follows. Section [S1](#) provides details on automated (non-spatial and spatial) exploratory data analysis related to the case study discussed in Sections [5](#). In Section [S2](#), we present the distributional results; Section [S2.1](#) provides the analytical derivation of the posterior predictive distribution in Equation [\(2.7\)](#) of Section [2.3](#), applicable to the spatial latent regression model in Equation [\(2.4\)](#). Section [S4](#) contains the computational details we examined. In Section [S4.1](#), we explicitly derive the objective function of the optimization problems described in Section [2.3](#). Moreover, in Section [S4.2](#), we offer a comprehensive discussion of the theoretical complexity, including comparisons with other algorithmic approaches. Section [S4.4](#) offers an innovative posterior sampling procedure for the regression coefficients β , which allows for improved memory allocation. Similarly, in Section [S4.3](#) we introduce an alternative algorithm for subset stacking, which is extremely efficient in large-scale problems. Finally, Section [S5.2](#) concludes the multivariate geospatial investigations with a sensitivity analysis on the subset dimension.

S1 Exploratory data analysis

This Section reports more exploratory analysis on Vegetation Index data presented in Section [5.1](#). Starting from the model-based non-spatial association among response variables, then concluding by presenting machine-generated supportive exploratory data insight used in Section [5](#).

Σ_{NDVI}	Σ_{RR}	$\rho_{\text{NDVI,RR}}$
0.2208 (0.2202, 0.2215)	0.1549 (0.1545, 0.1553)	-0.9049 (-0.9052, -0.9046)

Table S1: Non-spatial association between response variables. 50 (2.5, 97.5) quantile estimates using Bayesian multivariate linear regression.

We investigate non-spatial association between NDVI and red reflectance fitting the Bayesian multivariate regression model, defined by Equation (2.2). The model comprises two predictors: an intercept and the solar zenith angle for the million locations in the training set. More details on modeling and prior distribution are provided in Section 5, where a comparison of predictive performances is presented. Table S1 reports quantile estimates for marginal variances, i.e., the diagonal elements of Σ , and the correlation between NDVI and RR. Strong negative values for correlation are estimated, showing an intense inverse relationship between the two spatially dependent outcomes.

Hereafter, we present results from the fully automated explanatory spatial data analyses that complement Sections 5. Variograms are employed in both analyses to extract “guidelines” on spatial parameters such as spatial variability proportion α , and spatial range ϕ , which are essential for setting up the DOUBLE BPS framework for GeoAI applications. Variogram fitting, used to gather parameter values required for DOUBLE BPS, is fully automated and requires no human intervention, except for specifying the grid width.

We firstly use independent sample variograms for NDVI and RR, based on 31,875 randomly sampled locations. For NDVI, the empirical variogram estimates the nugget 0.03, a sill of 0.27, and a practical range of approximately 88 based upon automated weighted least squares. This corresponds to significant spatial correlation up to about 10,000 kilometers. The proportion of spatial variability is computed as $\alpha = \sigma^2 / (\tau^2 + \sigma^2) = 0.27 / (0.03 + 0.27) \approx 0.9$, resulting in 0.909 without rounding. Finally, the spatial range parameter is estimated as $\phi = 0.067$ based upon the distance beyond which the spatial correlation drops to less than 0.05; see the left panel of Figure S1.

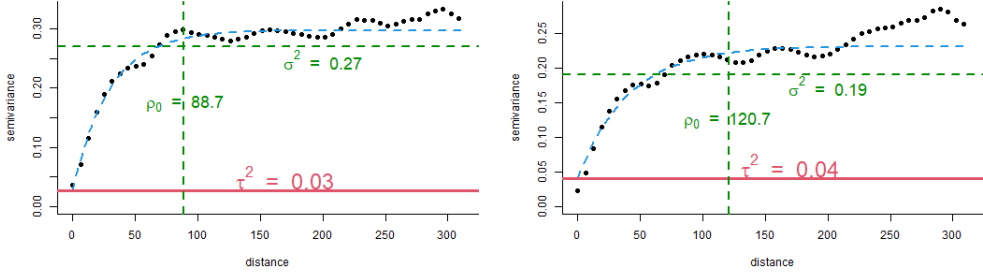


Figure S1: From left to right: sample variograms of NDVI, and Red Reflectance.

For RR, the variogram parameters include a nugget effect of 0.04, a sill of 0.19, and a practical range of approximately 120, which corresponds to around 13,000 kilometers. The slightly higher nugget effect for RR suggests greater measurement error or micro-scale variability compared to NDVI. The proportion of spatial variability is estimated as $\alpha = 0.19/(0.04 + 0.19) \approx 0.825$. The practical range for RR is more extended than that of NDVI, indicating that RR values remain spatially correlated over a greater distance. Concluding the exploratory spatial data analysis, we select a spatial range of $\phi = 0.049$ for RR.

The combined analysis of the variograms for NDVI and RR provides essential information about the spatial variance proportion and range parameters, which are critical for informing artificially intelligent geospatial modeling systems. This analysis results in $\alpha \in \{0.825, 0.909\}$ and $\phi \in \{0.049, 0.067\}$. These findings help improve the accuracy of spatial predictions, enhancing ecological interpretations and increasing computational efficiency by avoiding excessive misspecified model specifications.

The entire explanatory analysis workflow, designed to gather critical insights for improving the DOUBLE BPS methodology, is fully automated. Human input is then minimized; the only required user feed is the number of grid values for each spatial parameter.

Using the same subsample composed of 31,875 locations, we also investigated the cross-variogram; see Figure S2. This will help us extrapolate insights on spatial cross-dependencies.

The empirical cross-variogram depicts negative values, providing an estimate for the sill of -0.23 , and a practical range of approximately 85 based upon automated weighted least

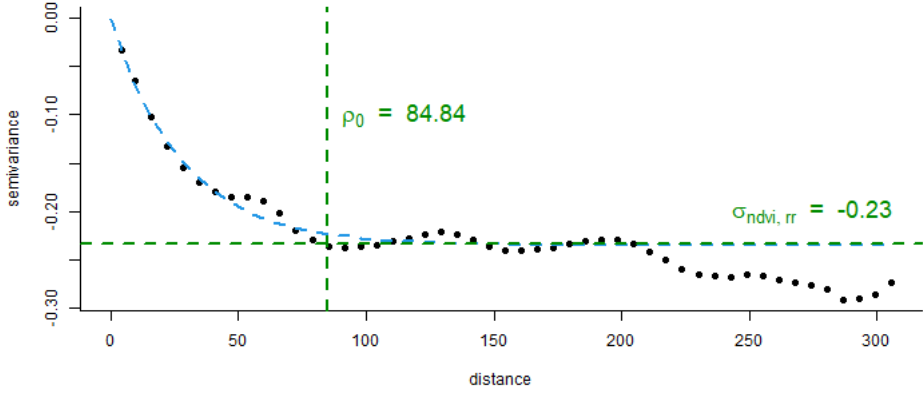


Figure S2: Sample cross-variogram between NDVI, and Red Reflectance.

squares. Similarly to individual variogram analysis, this shows a significant (negative) spatial correlation that withstands up to several thousand kilometers, suggesting a clear and well-defined negative spatial correlation structure between NDVI and red reflectance. Negative cross-variogram mirrors the negative correlation found using the non-spatial model (2.2). It is not surprising that the presence of strong (negative) spatial correlation among these indices, as their definition are strictly related, and both are based on spectral reflectance measurements acquired in the visible and near-infrared regions. Intuitively, the negative correlation emerged considering that healthy vegetation, which reflects high levels of biomass (NDVI), has strong chlorophyll absorption abilities, then revealing low red reflectance. Conversely, an increase in red reflectance corresponds to stressed (or low) vegetation, which results in low levels of the normalized difference vegetation index. Then non-spatial, and spatial negative association occurred are totally coherent with the nature of these indices and, coherent with literature (Tucker, 1979; Sellers, 1985).

S2 Distribution theory

S2.1 Posterior and predictive matrix-variate T distributions

The joint posterior predictive for $Y_{\mathcal{U}}$ and the unobserved latent process $\Omega_{\mathcal{U}}$, can be recast by integrating out $\{\gamma, \Sigma\}$ from the joint conditional posterior predictive, that is

$$p(Y_{\mathcal{U}}, \Omega_{\mathcal{U}} \mid \mathcal{D}) = \int \text{MN}_{n',q}(Y_{\mathcal{U}} \mid X_{\mathcal{U}}\beta + \Omega_{\mathcal{U}}, (\alpha^{-1} - 1)\mathbb{I}_{n'}, \Sigma) \times \text{MN}_{n',q}(\Omega_{\mathcal{U}} \mid M_{\mathcal{U}}\Omega, V_{\Omega_{\mathcal{U}}}, \Sigma) \\ \times \text{MNIW}(\gamma, \Sigma \mid \mu_{\gamma}^*, V_{\gamma}^*, \Psi^*, \nu^*) d\gamma d\Sigma,$$

where $M_{\mathcal{U}} = \rho_{\phi}(\mathcal{U}, \mathcal{S})\rho_{\phi}^{-1}(\mathcal{S}, \mathcal{S})$ and $V_{\Omega_{\mathcal{U}}} = \rho_{\phi}(\mathcal{U}, \mathcal{U}) - \rho_{\phi}(\mathcal{U}, \mathcal{S})\rho_{\phi}^{-1}(\mathcal{S}, \mathcal{S})\rho_{\phi}(\mathcal{S}, \mathcal{U})$. We derive $p(\Omega_{\mathcal{U}}, Y_{\mathcal{U}} \mid \Sigma, \mathcal{D})$ by avoiding direct integration with respect to γ using the following augmented linear system

$$\underbrace{\begin{bmatrix} \Omega_{\mathcal{U}} \\ Y_{\mathcal{U}} \end{bmatrix}}_{\Upsilon} = \underbrace{\begin{bmatrix} 0_{n' \times q} & M_{\mathcal{U}} \\ X_{\mathcal{U}} & M_{\mathcal{U}} \end{bmatrix}}_M \underbrace{\begin{bmatrix} \beta \\ \Omega \end{bmatrix}}_{\gamma} + \underbrace{\begin{bmatrix} E_{Y_{\mathcal{U}}} \\ E_{\Omega_{\mathcal{U}}} \end{bmatrix}}_E, \quad E \sim \text{MN}_{2n',q}(0_{2n' \times q}, V_E, \Sigma), \quad (\text{S1})$$

where $V_E = \begin{bmatrix} V_{\Omega_{\mathcal{U}}} & V_{\Omega_{\mathcal{U}}} \\ V_{\Omega_{\mathcal{U}}} & (\alpha^{-1} - 1)\mathbb{I}_{n'} + V_{\Omega_{\mathcal{U}}} \end{bmatrix}$. We write the posterior distribution $p(\gamma \mid \mathcal{D})$ in Equation (2.6) as a linear equation, $\gamma = \mu_{\gamma}^* + E_{\gamma}$, with $E_{\gamma} \sim \text{MN}_{n',q}(O, V_{\gamma}^*, \Sigma)$, where E and E_{γ} are independent of each other. Then,

$$\Upsilon = M\mu_{\gamma}^* + ME_{\gamma} + E \sim \text{MN}_{2n',q}(M\mu_{\gamma}^*, V^*, \Sigma), \quad (\text{S2})$$

where $V^* = MV_{\gamma}^*M^{\top} + V_E$. This yields $p(\Upsilon \mid \Sigma, \mathcal{D}) = p(\Omega_{\mathcal{U}}, Y_{\mathcal{U}} \mid \Sigma, \mathcal{D})$ as the closed-form joint predictive distribution by integrating out Σ from $p(\Omega_{\mathcal{U}}, Y_{\mathcal{U}} \mid \Sigma, \mathcal{D})p(\Sigma \mid \mathcal{D})$ to get

$$\int \text{MNIW}(\Omega_{\mathcal{U}}, Y_{\mathcal{U}}, \Sigma \mid M\mu_{\gamma}^*, V^*, \Psi^*, \nu^*) d\Sigma = \text{T}_{2n',q}(\nu^*, M\mu_{\gamma}^*, V^*, \Psi^*)$$

which is a matrix-variate Student's t random variable. Defining $\Upsilon = [\Omega_{\mathcal{U}}^T, Y_{\mathcal{U}}^T]^T$, as a matrix of dimension $m \times q$, where $m = 2n'$, the predictive distribution is

$$p(\Upsilon \mid Y) = \int P(\Upsilon, \Sigma \mid Y) d\Sigma . \quad (\text{S3})$$

This matrix-variate integral can be avoided by simply writing

$$p(\Upsilon \mid Y) = \frac{p(\Upsilon, \Sigma \mid Y)}{p(\Sigma \mid \Upsilon, Y)}. \quad (\text{S4})$$

The density $p(\Upsilon, \Sigma \mid Y)$ comes from Equation (S2), while the denominator is obtained as

$$\begin{aligned} p(\Sigma \mid \Upsilon, Y) &= \frac{p(\Sigma \mid Y)p(\Upsilon \mid \Sigma, Y)}{p(\Upsilon \mid Y)} \\ &\propto \frac{|\Psi^*|^{\frac{\nu^*}{2}} |V_{\gamma}^*|^{-\frac{q}{2}} |\Sigma|^{-\frac{\nu^*+m+q+1}{2}}}{2^{\frac{(\nu^*+m)q}{2}} (\pi)^{\frac{mq}{2}} \Gamma_q\left(\frac{\nu^*}{2}\right)} \exp\left\{-\frac{1}{2} \text{tr} [\Sigma^{-1} (\Psi^* + (\Upsilon - \mu^*)^T V_{\gamma}^{\star-1} (\Upsilon - \mu^*))]\right\} \\ &\propto |\Sigma|^{-\frac{\nu^*+m+q+1}{2}} \exp\left\{-\frac{1}{2} \text{tr} [\Sigma^{-1} (\Psi^* + (\Upsilon - \mu^*)^T V_{\gamma}^{\star-1} (\Upsilon - \mu^*))]\right\}, \end{aligned}$$

where $\mu^* = M\mu_{\gamma}^*$. Hence, $\Sigma \mid \Upsilon, Y \sim \text{IW}(\hat{\Psi}, \hat{\nu})$ with $\hat{\Psi} = (\Psi^* + (\Upsilon - \mu^*)^T V_{\gamma}^{\star-1} (\Upsilon - \mu^*))$, and $\hat{\nu} = \nu^* + m$. The joint posterior predictive density by the follows from Equation (S4)

$$\begin{aligned} p(\Upsilon \mid Y) &= \frac{\text{MNIW}(\Upsilon, \Sigma \mid \mu^*, V_{\gamma}^*, \Psi^*, \nu^*)}{\text{IW}(\Sigma \mid \hat{\Psi}, \hat{\nu})} \\ &= K(\Upsilon) |\Psi^*|^{-\frac{\nu^*+m}{2}} |\mathbb{I}_m + V_{\gamma}^{\star-1} (\Upsilon - \mu^*) \Psi^{\star-1} (\Upsilon - \mu^*)^T|^{-\frac{\nu^*+m}{2}}, \end{aligned}$$

$$\text{where } K(\Upsilon) = \frac{\Gamma_q\left(\frac{\hat{\nu}}{2}\right) |\Psi^*|^{\frac{\nu^*}{2}} |V_{\gamma}^*|^{-\frac{q}{2}}}{\Gamma_q\left(\frac{\nu^*}{2}\right) (\pi)^{\frac{mq}{2}}} = \frac{\Gamma_q\left(\frac{\nu^*+m}{2}\right) |\Psi^*|^{\frac{\nu^*}{2}} |V_{\gamma}^*|^{-\frac{q}{2}}}{\Gamma_q\left(\frac{\nu^*}{2}\right) (\pi)^{\frac{mq}{2}}}, \text{ since } \hat{\nu} = \nu^* + m.$$

This is a matrix-variate T density, which we denote as $\Upsilon \mid Y \sim \text{T}_{m,q}(\nu^*, \mu^*, V^*, \Psi^*)$. We recover exactly the same result, without needing to integrate out Σ (Iranmanesh et al., 2010; Gupta and Nagar, 2000), but only using Bayes theorem and related distribution theory. Finally, the marginal predictive distributions $\Omega_{\mathcal{U}} \mid \mathcal{D}$, and $Y_{\mathcal{U}} \mid \mathcal{D}$, are also available in analytic form as matrix T distributions for any set of predictive points \mathcal{U} .

S3 Asymptotic behaviors

The DOUBLE BPS extends the Bayesian predictive stacking to a transfer learning framework, as detailed in Section 2.3. Now, we assess the asymptotic behavior of its approximation in terms of predictive distributions. Specifically, we investigate how the DOUBLE BPS approximations of posterior predictive distributions behave when the number of competitive models (J) and the number of partitions (K) grow towards infinity. We focus on the reversed Kullback-Leibler divergence between the DOUBLE BPS posterior predictive in (2.11) and the true one $p_t(\cdot | \mathcal{D})$, defined in Equation (2.7) where $\{\alpha, \phi\}$ are those of the data-generating process.

Applying Jensen's inequality, we derive an upper bound for the reverse KL divergence; further details, including derivations and implementations, are provided in Sections S3.1 and S3.2. The resulting upper bound is as follows.

$$D_{KL}(\hat{P} \| P_t) \leq \log \prod_{k=1}^K \left\{ \sum_{k=1}^K \hat{w}_k \sum_{j=1}^J \hat{z}_{k,j} \mathbb{E}_{\hat{p}_{k,j}} \left[\frac{\sum_{j=1}^J \hat{p}(y | \mathcal{D}_k, \mathcal{M}_j)}{p_t(y | \mathcal{D})} \right] \right\}^{\hat{w}_k}, \quad (\text{S5})$$

where \hat{P} and P_t denote probability measures with probability density $\hat{p}(\cdot ; \mathcal{D})$, and $p_t(\cdot | \mathcal{D})$, respectively, and $\hat{p}_{k,j} = \hat{p}(\cdot | \mathcal{D}_k, \mathcal{M}_j)$.

The upper bound in (S5) can be analyzed both analytically and empirically. In Section S3.2, we provide a Monte Carlo study that approximates the expected value and explore how the bound varies with the number of subsets (K) and the number of candidate models (J).

S3.1 Kullback-Leibler divergence from true posterior predictive

The true predictive distribution is defined as: $p_t(y | \mathcal{D}) = p(y | \mathcal{D}, \alpha_t, \phi_t) = T(\nu_t, M_t, V_t, \Psi_t)$, while the DOUBLE BPS approximation is:

$$\begin{aligned}\hat{p}(y ; \mathcal{D}) &= \sum_{k=1}^K \hat{w}_k \sum_{j=1}^J \hat{z}_{k,j} p(y | \mathcal{D}_k, \alpha_j, \phi_j) \\ &= \sum_{k=1}^K \hat{w}_k \sum_{j=1}^J \hat{z}_{k,j} T(y | \nu_{k,j}, M_{k,j}, V_{k,j}, \Psi_{k,j}).\end{aligned}$$

Let \hat{P} and P_t be the probability distributions corresponding to the DOUBLE BPS approximate and the true predictive probability distributions, respectively. The reverse KL divergences is given by:

$$D_{\text{KL}}(\hat{P} \| P_t) = \int_y \log \frac{\hat{P}(\mathrm{d}y)}{P_t(\mathrm{d}y)} \hat{P}(\mathrm{d}y) = \int_{y \in \mathbb{R}^{n \times q}} \sum_{k=1}^K \hat{w}_k \hat{p}_k(y | \mathcal{D}_k) \log \frac{\sum_{k=1}^K \hat{w}_k \hat{p}_k(y | \mathcal{D}_k)}{p_t(y | \mathcal{D})} \mathrm{d}y,$$

where $\hat{p}_k(y ; \mathcal{D}_k) = \sum_{j=1}^J \hat{z}_{k,j} T(y | \nu_{k,j}, M_{k,j}, V_{k,j}, \Psi_{k,j})$. We can reformulate this Equation as the difference of two expectations:

$$\begin{aligned}&\sum_{k=1}^K \hat{w}_k \mathbb{E}_{\hat{p}_k} \left[\log \sum_{k=1}^K \hat{w}_k \hat{p}_k(y ; \mathcal{D}_k) \right] - \sum_{k=1}^K \hat{w}_k \mathbb{E}_{\hat{p}_k} \left[\log p_t(y | \mathcal{D}) \right] \\ &= \sum_{k=1}^K \hat{w}_k \mathbb{E}_{\hat{p}_k} \left[\log \frac{\sum_{k=1}^K \hat{w}_k \hat{p}_k(y ; \mathcal{D}_k)}{p_t(y | \mathcal{D})} \right] \\ &\leq \sum_{k=1}^K \hat{w}_k \log \mathbb{E}_{\hat{p}_k} \left[\frac{\sum_{k=1}^K \hat{w}_k \hat{p}_k(y ; \mathcal{D}_k)}{p_t(y | \mathcal{D})} \right],\end{aligned}$$

where the inequality follows from Jensen's inequality. Expanding algebraically, this term, we get the more convenient formulation in Equation (S5).

S3.2 Monte Carlo approximation for upper bound simulations

We perform empirical investigations of the upper bound presented in Section S3, and detailed in Section S3.1, for different values of K , and J ceteris paribus.

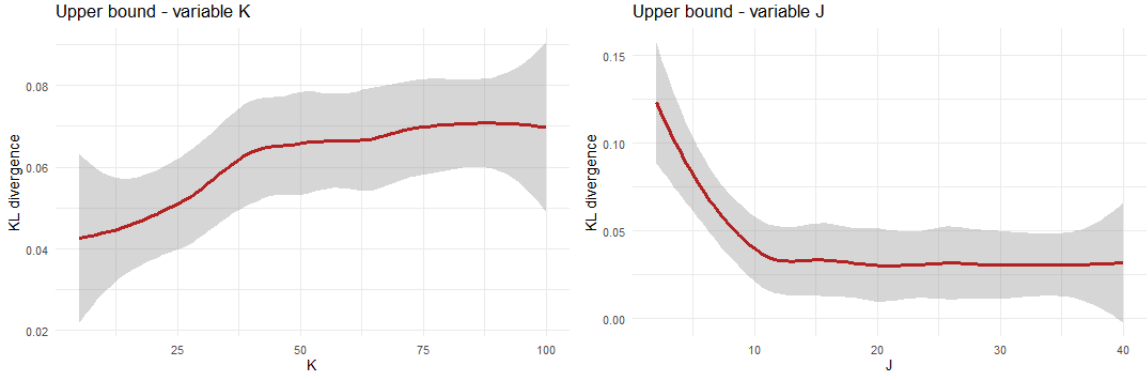


Figure S3: Upper bound behave for growing values of K , and J

We approach the problem of approximating the expectation in Equation (S5) with a Monte Carlo integration. The approximation takes the form

$$\mathbb{E}_{\hat{p}_{k,j}} \left[\frac{\sum_{j=1}^J \hat{p}(y \mid \mathcal{D}_k, \mathcal{M}_j)}{p_t(y \mid \mathcal{D})} \right] \approx \frac{1}{L} \sum_{l=1}^L \left[\frac{\sum_{j=1}^J \hat{p}(y_l \mid \mathcal{D}_k, \mathcal{M}_j)}{p_t(y_l \mid \mathcal{D})} \right],$$

where $y_l \sim \hat{p}(y_l \mid \mathcal{D}_k, \mathcal{M}_j)$ for $l = 1, \dots, L$. We then devise the Algorithm S1 to approximate the upper bound for the KL divergence between the DOUBLE BPS posterior predictive and the true one.

To provide a meaningful interpolation, we consider 20 points for each parameter regulating $\hat{u}b(n, K, J)$. We let vary $K \in \{5, 100\}$, $J \in \{2, 40\}$, while $n = 1000$ was fixed. Then, we remove data dependency by considering $M = 10$ replications for each evaluation setting. We perform different simulations for any of $\{K, J\}$ ceteris paribus, for the other. The panels in Figure S3 shows how $D_{KL}(\hat{P} \parallel P_t)$ vary with K , and J , respectively.

S4 Computational details

Key computational aspects of the proposed method involve two points: comparing its theoretical complexity to state-of-the-art approaches and addressing memory constraints. The complexity comparison evaluates the method's time and space efficiency, particularly its scalability with larger datasets. This includes discernment from the explicit objective function,

Algorithm S1 Approximating upper bound for Kullback-Liebler divergence

Input: Y outcomes matrix; X predictors matrix; $\hat{w} = \{\hat{w}_k : k = 1, \dots, K\}$: Stacking weights between subsets; $\hat{z} = \{\hat{z}_k = \{\hat{z}_{k,j}\} : k \in \{1, \dots, K\}, j \in \{1, \dots, J\}\}$: Stacking weights within subsets; $\hat{p}_{k,j}(\cdot), p_t(\cdot)$ approximated and true predictive distributions $\forall j = 1, \dots, J, k = 1, \dots, K$; K : Number of subsets; J : number of competitive models in each subset; n : number of locations; L : number of Monte Carlo samples.

Output: $\hat{ub}(n, K, J)$: approximated value for the upper bound, for a given set $\{n, K, J\}$.

```

1: for  $k = 1, \dots, K$  do
2:   for  $j = 1, \dots, J$  do
3:     Draw  $L$  samples  $\{y_l : l = 1, \dots, L\}$  from  $\hat{p}(\cdot | \mathcal{D}_k, \mathcal{M}_j)$ 
4:     for  $l = 1, \dots, L$  do
5:       for  $j = 1, \dots, J$  do
6:         Evaluate  $p_{k,j,l} = \hat{p}(y_l | \mathcal{D}_k, \mathcal{M}_j)$ 
7:       end for
8:       Evaluate  $p_{t,l} = p(y_l | \mathcal{D})$ 
9:       Compute  $r_l = \frac{\sum_{j=1}^J z_{k,j} p_{k,j,l}}{p_{t,l}}$ 
10:      end for
11:      Compute  $e_{k,j} = \frac{1}{L} \sum_{l=1}^L r_l$ 
12:    end for
13:  end for
14:  Compute  $c_k = \sum_{k=1}^K \hat{w}_k \sum_{j=1}^J \hat{z}_{k,j} e_{k,j}$ 
15: return  $\hat{ub}(n, K, J) = \log \prod_{k=1}^K c_k^{\hat{w}_k}$ 

```

highlighting its computational impact. Memory constraints are equally critical, as limitations can hinder performance despite powerful processors. The proposed method addresses these challenges, ensuring both scalability and efficient resource use.

In summary, this section will examine both the theoretical complexity, including the explicit derivation of the objective function for the optimization problems detailed in Equations (2.8) and (S6), as well as the memory management strategies, offering a comprehensive view of the computational feasibility in practical applications.

S4.1 Objective function for double Bayesian predictive stacking

We expound the double Bayesian predictive stacking in Section 2.3. The optimization problem used to compute the stacking weights in Equation (2.10) is formally defined as:

$$\max_{w \in S_1^K} \frac{1}{n} \sum_{i=1}^n \log \sum_{k=1}^K w_k \hat{p}(Y_i ; \mathcal{D}_k) = \max_{w \in S_1^K} \frac{1}{n} \sum_{i=1}^n \log \sum_{k=1}^K w_k \sum_{j=1}^J \hat{z}_{k,j} p(Y_{k,i} | \mathcal{D}_{k,[-l]}, \mathcal{M}_j), \quad (\text{S6})$$

as $\hat{p}(Y_i ; \mathcal{D}_k) = \sum_{j=1}^J \hat{z}_{k,j} p(Y_{k,i} | \mathcal{D}_{k,[-l]}, \mathcal{M}_j)$. In this DOUBLE BPS framework, we focus exclusively on \mathcal{D}_k , which is treated equivalently to \mathcal{M}_j in the first step. It is crucial to discriminate the predictive performance induced by each \mathcal{D}_k . We must utilize a common set of Y across all \mathcal{D}_k – namely, Y itself. This stems from the construction of DOUBLE BPS. Specifically, for DOUBLE BPS to be effective, it necessitates predictive assessments over a common set of points for each model in the competition. Otherwise, the predictive performances cannot be directly compared, and the weights cannot be optimized to distinguish predictive capabilities across models, as different points would be used for different models. To illustrate, consider the first stacking step. Here, we compute $p(Y_{k,i} | \mathcal{D}_k, \mathcal{M}_j)$ for each subset, where $i = 1, \dots, n_k$ and $j = 1, \dots, J$. This allows us to evaluate Y_k with respect to the predictive density of all J models under comparison. Similarly, in DOUBLE BPS, the goal is to evaluate Y_i with respect to the predictive density across all K subsets (acting as competing models) for comparison. The weights $\{\hat{z}_{k,j}\}$, which are derived from the optimization problem specified in Equation (2.8) also appear in Equation (S6). However, comparing the right-hand sides of Equations (S6) and (2.8), we observe that the objective functions are almost identical, with the only difference being the second convex linear combination governed by the weights $\{w_k\}$. Therefore, the predictive distributions in both optimization problems refer to the same quantity. To summarize, the objective function in Equation (2.8) can be derived by substituting each $\{z_{k,j}\}$ with its optimized counterpart $\{\hat{z}_{k,j}\}$ and incorporating the weights $\{w_k\}$. This leads to the maximization objective in Equation (S6).

Next, we consider the optimization problem in Equation (2.8) with objective function,

$$\max_{z_k \in S_1^J} \frac{1}{n_k} \sum_{i=1}^{n_k} \log \sum_{j=1}^J z_{k,j} p(Y_{k,i} \mid \mathcal{D}_{k,[-l]}, \mathcal{M}_j) = \max_{z_k \in S_1^J} f(z_k), \quad (\text{S7})$$

where $f(z_k) = \frac{1}{n_k} \sum_{i=1}^{n_k} \log \sum_{j=1}^J z_{k,j} p(Y_{k,i} \mid \mathcal{D}_{k,[-l]}, \mathcal{M}_j)$. An explicit form of $f(z_k)$ is

$$\begin{aligned} f(z_k) &= f(z_{k,1}, \dots, z_{k,J}) = \frac{1}{n_k} \sum_{i=1}^{n_k} \log \sum_{j=1}^J z_{k,j} p(Y_{k,i} \mid \mathcal{D}_{k,[-l]}, \mathcal{M}_j) \\ &= \frac{1}{n_k} \sum_{i=1}^{n_k} \log \sum_{j=1}^J z_{k,j} T_{1,q}(Y_{k,i} \mid \nu_{[-l]}^*, \mu_i^*, V_i^*, \Psi_{[-l]}^*) \\ &= \frac{1}{n_k} \sum_{i=1}^{n_k} \log \sum_{j=1}^J z_{k,j} K(Y_{k,i}) \left| 1 + V_i^{*-1}(Y_{k,i} - \mu_i^*) \Psi_{[-l]}^{-1*}(Y_{k,i} - \mu_i^*)^T \right|^{-\frac{\nu_{[-l]}^*+1}{2}}, \end{aligned} \quad (\text{S8})$$

where $K(Y_{k,i}) = \frac{|\Psi_{[-l]}^*|^{-\frac{1}{2}} |V_i^*|^{-\frac{q}{2}} \Gamma_q\left(\frac{\nu_{[-l]}^*+1}{2}\right)}{(\pi)^{\frac{1}{2}} \Gamma_q\left(\frac{\nu_{[-l]}^*}{2}\right)}$. The logarithm of a linear combination precludes further accessibility, but $f(z_k)$ is computed easily by evaluating the matrix-T density. This is standard convex optimization (Yao et al., 2018); see Section 3 for further details.

The objective function in Equation (S6) is related to Equation (2.8) as

$$\max_{w \in S_1^K} \frac{1}{n} \sum_{i=1}^n \log \sum_{k=1}^K w_k \sum_{j=1}^J \hat{z}_{k,j} p(Y_{k,i} \mid \mathcal{D}_{k,[-l]}, \mathcal{M}_j) = \max_{w \in S_1^K} g(w), \quad (\text{S9})$$

where $w = (w_1, \dots, w_K)^T$ and

$$\begin{aligned} g(w) &= \frac{1}{n} \sum_{i=1}^n \log \sum_{k=1}^K w_k \sum_{j=1}^J \hat{z}_{k,j} p(Y_{k,i} \mid \mathcal{D}_{k,[-l]}, \mathcal{M}_j) \\ &= \frac{1}{n} \sum_{i=1}^n \log \sum_{k=1}^K w_k \sum_{j=1}^J \hat{z}_{k,j} T_{1,q}(Y_{k,i} \mid \nu_{[-l]}^*, \mu_i^*, V_i^*, \Psi_{[-l]}^*) \\ &= \frac{1}{n} \sum_{i=1}^n \log \sum_{k=1}^K w_k \sum_{j=1}^J \hat{z}_{k,j} K(Y_{k,i}) \left| 1 + V_i^{*-1}(Y_{k,i} - \mu_i^*) \Psi_{[-l]}^{-1*}(Y_{k,i} - \mu_i^*)^T \right|^{-\frac{\nu_{[-l]}^*+1}{2}}. \end{aligned} \quad (\text{S10})$$

In practical applications, we address Equation (S6) separately from Equation (2.8), which is defined for each k^{th} subset. Although it must be solved for each subset, we perform K

separate maximizations of Equation (2.8), one for each subset. Once we obtain all K sets of $\{\hat{z}_{k,j}\}$, we can recover the weights $\{\hat{w}_k\}$ across subsets by solving the convex optimization problem in Equation (S6).

Overlooking the possibility of computing the subset stacking weights $\{z_{k,j}\}$ in parallel for the time being, this method offers a significant computational benefit: no extra quantities need to be computed to solve the problem in Equation (S6). All necessary information is already available from independent computations performed within each subset. For clarity, all the terms in Equations (2.8) and (S6) are known and coincide except for the weights w , which still need to be optimized. Consequently, there is no need to recompute the cross-validated predictive distributions or $\{\hat{z}_{k,j}\}$ as all these components have been computed.

S4.2 Theoretical complexity

In terms of theoretical computational complexity, we provide a comparison between spatial meta-kriging (SMK [Guhaniyogi and Banerjee, 2018](#)) and the double DOUBLE BPS. So far, given a dataset \mathcal{D}_n , n denotes the total number of observations and K the number of subsets. Let M be the number of target posterior samples. From [Guhaniyogi and Banerjee \(2018\)](#), it is known that each posterior sample, considering a parallel implementation over K cores of SMK requires $\mathcal{O}\left(\left(\frac{n}{K}\right)^3\right)$. Thus, taking into account M draws from each of the subset posteriors yields theoretical complexity of $\mathcal{O}\left(M\left(\frac{n}{K}\right)^3\right)$, for each computational core. The cost of computing the Geometric median also has to be added. As stated in [Minsker et al. \(2017\)](#), Weiszfeld's algorithm has a complexity of $\mathcal{O}(M^2)$ for each step, and it needs at most $\mathcal{O}(1/\epsilon)$ steps to approximate the full posterior to a degree ϵ of accuracy. However, especially in large-scale applications, having a computational core for each subset is not always possible. Let us consider the number of available cores hereafter as m , generally $m << K$. Leading the total complexity of SMK, for K partitions in parallel over m cores to $\mathcal{O}\left(\frac{K}{m}\left[M\left(\frac{n}{K}\right)^3\right] + \frac{(KM)^2}{\epsilon}\right)$.

For theoretical complexity of double Bayesian predictive stacking, we have to specify J as the number of competitive models, and L as the number of folds used for cross-validations. Equivalently to SMK, model fitting within subsets is dominated by Cholesky decompositions implying costs in the order of $\mathcal{O}\left((\frac{n}{K})^3\right)$. Nevertheless, in DOUBLE BPS, we perform J Cholesky decompositions, and for each of them, we refit the model L times. Hence, the theoretical complexity boils down to $\mathcal{O}\left(\frac{K}{m}JL\left(\frac{\ell n}{K}\right)^3\right)$. In addition, we use the package CVXR [Fu et al. \(2020\)](#) in the R statistical computing environment by applying disciplined convex programming [Grant \(2005\)](#); [CVX Research \(2012\)](#) to find the stacking weights in polynomial time using an interior-point algorithm. We used the solvers SCS ([O'Donoghue et al., 2016](#)) and ECOSolveR ([Fu and Narasimhan, 2023](#)) to obtain the stacking weights. This introduces the discipline convex problems into the theoretical complexity, turning out to be $\mathcal{O}\left(\frac{K}{m}[JL\left(\frac{n}{K}\right)^3 + J^p] + K^p\right)$, for K subsets over m cores, and a polynomial degree p . The portion in square brackets pertains to model fitting within each subset, consisting of a term related to cross-validation and the polynomial cost of DOUBLE BPS across J models. Finally, we account for the complexity introduced by the second stacking process across the K subsets.

Next, we compare the computational complexities of the two approaches. We will separately examine the terms associated with subset modeling and global inference combination. Thus, for SMK and DOUBLE BPS, respectively, the computational complexities are as follows:

$$\mathcal{O}\left(\frac{K}{m}\underbrace{\left[M\left(\frac{n}{K}\right)^3\right]}_{\text{subset modeling}} + \underbrace{\frac{(KM)^2}{\epsilon}}_{\text{combination}}\right), \quad \mathcal{O}\left(\frac{K}{m}\underbrace{\left[JL\left(\frac{\ell n}{K}\right)^3 + J^p\right]}_{\text{subset modeling}} + \underbrace{K^p}_{\text{combination}}\right) \quad (\text{S11})$$

Focusing on the subset modeling component, as highlighted in Equation (S11), two key specifications stand out. First, consider the difference in magnitude between M and the product JL . In this context, DOUBLE BPS offers a theoretical advantage when $JL < M$, a quite common condition in practice. This is because M represents the number of posterior

samples required for convergence across all the Markov chains involved, and it typically needs to be at least on the order of 10^3 . In contrast, the product JL consists of relatively small terms, making it highly likely that this inequality will hold. Second, due to the significant difference in scale, the term J^p is absorbed by $(n/K)^3$

When comparing the combination phase, the analysis reduces to a comparison between the geometric median approximation and Bayesian predictive stacking. Since a discrete number of posterior samples M is required by SMK for each of the K partitions, we generally find that $K^p < (KM)^2/\epsilon$. Thus, while empirical computational times are significantly lower for double Bayesian predictive stacking compared to SMK, there are some modest theoretical differences between the two methods. The major advantage lies in avoiding simulation-based methods, such as MCMC while achieving local inferences through exact approaches.

Like Weiszfeld's algorithm, modern disciplined convex programming encounters computational challenges in high-dimensional contexts, particularly in managing random memory allocation. In Section [S4.3](#), we present a feasible strategy for approximating the DOUBLE BPS weights, tailored for very large-scale memory problems.

S4.3 Memory management and Pseudo-BMA

When modeling GeoAI systems, as the number of locations exceeds the order of millions, managing storage space becomes crucial. Timing issues may arise depending on the available optimizer. While open-source solvers theoretically offer faster solutions compared to iterative algorithms, e.g. geometric median, they often face practical challenges when the problem size considerably exceeds dimensions of 10^2 . In contrast, commercial optimizers behave slightly better, even if these approaches are not exempted from random allocation memory constraints. We emphasize working with portable approaches, i.e. with open-source solvers, that can effectively handle large-scale problems.

Algorithm S2 Calculating stacking weights between subsets using pseudo-BMA

Input: $\hat{z} = \{\hat{z}_k = \{\hat{z}_{k,j}\} : k \in \{1, \dots, K\}, j \in \{1, \dots, J\}\}$: Stacking weights within subsets; $\{pd_{k,j,i} = T_{1,q}(Y_{k,i} \mid \nu_{[-l]}^*, \mu_i^*, V_i^*, \Psi_{[-l]}^*) : k = 1, \dots, K, j = 1, \dots, J, i = 1, \dots, n\}$: point-wise predictive density of Y ; n, q, p : Number of rows, number of outcomes, and number of predictors; $K, \{n_k : k \in \{1, \dots, K\}\}, J$: Number of subsets, dimension of each subset, and number of competitive models in each subset.

Output: $\hat{w} = \{\hat{w}_k : k = 1, \dots, K\}$: Stacking weights between subsets.

1: Construct $pd = \underbrace{[pd_1^T : \dots : pd_K^T]}_{n \times J}^T$, $pd_k = \underbrace{\begin{bmatrix} pd_{k,1,1} & \dots & pd_{k,J,1} \\ \vdots & pd_{k,j,i} & \vdots \\ pd_{k,1,n_k} & \dots & pd_{k,J,n_k} \end{bmatrix}}_{n_k \times J}$

2: **for** $k = 1, \dots, K$ **do**

3: Compute $\widehat{elpd}^k = \sum_{i=1}^n \log (pd \hat{z}_k)$

4: **end for**

5: **for** $k = 1, \dots, K$ **do**

6: Compute $\hat{w}_k = \exp(\widehat{elpd}^k) / \sum_{k=1}^K \exp(\widehat{elpd}^k)$

7: **end for**

8: **return** $\hat{w} = \{\hat{w}_k : k \in \{1, \dots, K\}\}$

We present a computationally cheaper alternative that facilitates better management of available RAM. The subsequent contents, including Algorithm S2, were implemented in data analyses involving millions (10^6) of locations of Section 5. When addressing optimization problems of significant dimensions, AIC-based alternatives could be considered.

To facilitate model stacking, various methodologies exist within the Bayesian model averaging (BMA) framework. In particular, we present an approach based on information criteria, and formerly introduced in Yao et al. (2018). To ensure comparability between datasets and enhance interpretability, we estimate the expected log point-wise predictive density (as done in DOUBLE BPS). The expected log pointwise predictive density ($elpd$) for each partition k is defined as

$$\widehat{elpd}^k = \sum_{i=1}^n \widehat{elpd}_i^k = \sum_{i=1}^n \log p(Y_{k,i} \mid \mathcal{D}_{k,[-l]}) \quad (\text{S12})$$

Importantly, each $elpd$ term need not be computed individually, as these values are generated during the first BPS procedure within each subset for all model configurations, significantly reducing memory storage requirements and the total computational burden. Given the set $\{\widehat{elpd}^k\}_{k=1, \dots, K}$, the pseudo Bayesian model averaging (pseudo-BMA) weights are computed

as

$$\hat{w}_k = \frac{\exp(\widehat{\text{elpd}}^k)}{\sum_{k=1}^K \exp(\widehat{\text{elpd}}^k)}. \quad (\text{S13})$$

This formulation, early introduced by [Yao et al. \(2018\)](#), simplifies the computation of the stacking weights, significantly reducing computational costs in terms of complexity and storage while maintaining the Bayesian predictive stacking framework. Thus, it serves as a viable alternative to BPS for predictive densities in challenging scenarios. When dealing with datasets comprising millions of instances and a substantial number of partitions, optimization solvers may fail or produce errors due to memory constraints, and the iterative processes involving large matrices can lead to increased procedure times.

Based on empirical experience, we primarily utilize pseudo-BMA as a Bayesian predictive stacking approach when datasets require excessive memory storage, particularly when $n \gg 10^5$ and $K \gg 10^2$. When feasible we generally prefer convex optimization using BPS of predictive densities without reservations. Simulations highlighting potential differences in posterior predictive and posterior inference performances between these two model stacking approaches can be found in [Yao et al. \(2018\)](#), where several alternatives to Bayesian stacking approaches were discussed. We opted for pseudo-BMA due to its simpler analytical formulation, which enables matrix algebra to mitigate the computational burden of both random allocation memory and runtime.

S4.4 Memory-efficient posterior sampling

In the matrix-variate conjugate Bayesian linear regression model presented in Equation (2.2), the Bayesian updating process may become costly if several data shards come, even more, if the dimensions involved are somehow cumbersome. Computational problems are often related to the available RAM, especially when working with considerable datasets. We present a memory-efficient posterior sampling for the regression coefficient β , helping in such intricate

contexts. We consider the model in Equation (2.2) of Section 2.1,

$$\begin{aligned} Y &= X\beta + E, \quad E \mid \Sigma \sim \text{MN}(O, V, \Sigma); \\ \beta &= M_0m_0 + E_\beta, \quad E_\beta \mid \Sigma \sim \text{MN}(O, M_0, \Sigma); \quad \Sigma \sim \text{IW}(\Psi_0, \nu_0), \end{aligned} \quad (\text{S14})$$

Where Σ is assumed as known hereafter. Then, by matrix normal distribution theory, we know the exact form of the posterior distribution

$$\beta \mid \mathcal{D}, \Sigma \sim \text{MN}(M_n m_n, M_n, \Sigma), \quad (\text{S15})$$

where $M_n^{-1} = M_0^{-1} + X^\top V^{-1} X$, $m_n = m_0 + X^\top V^{-1} Y$. We provide a memory-efficient way to sample from this distribution and reduce its computational burden. We define random variables $Y_{rep} \sim \text{MN}(Y, V, \Sigma)$ and $Z \sim \text{MN}(M_0 m_0, M_0, \Sigma)$. Expressing the relation between Y_{rep} , Z , and B as

$$M_n^{-1} B = A_1 Z + A_2 Y_{rep}. \quad (\text{S16})$$

We seek matrices A_1, A_2 such that $B \stackrel{d}{=} \beta \mid \mathcal{D}, \Sigma$. Since $\beta \mid \mathcal{D}, \Sigma$ is distributed as a Gaussian random variable, it is fully characterized by its mean and variance (in a such case, with both row and column covariance matrices). Then, all we need are A_1 and A_2 so that the first two moments of B matches with $\beta \mid \mathcal{D}, \Sigma$.

For $X \sim \text{MN}(m, v, s)$, we have $DXC \sim \text{MN}(DmC, DvD^\top, CsC^\top)$. Moreover, if X is $n \times q$, the row-variance matrix is defined as $v = \mathbb{V}_{row}(X) = \mathbb{E}[(X - m)(X - m)^\top] \text{tr}(s)^{-1}$ of dimension $(n \times n)$ and its elements are defined as the variance computed on each row, while the $q \times q$ column covariance matrix is depicted by $s = \mathbb{V}_{col}(X) = \mathbb{E}[(X - m)^\top(X - m)] \text{tr}(v)^{-1}$ (see, e.g., [Gupta and Nagar, 2000](#), for further details). Without loss of generality, we compute the row covariance matrix for B since the column covariance matrix Σ is given. Note that

$$M_n^{-1} \mathbb{V}_{row}(B) M_n^{-1} = A_1 \mathbb{V}_{row}(Z) A_1^\top + A_2 \mathbb{V}_{row}(Y_{rep}) A_2^\top = A_1 M_0 A_1^\top + A_2 V A_2^\top \quad (\text{S17})$$

Setting these matrices as $A_1 = M_0^{-1}$, and $A_2 = X^\top V^{-1}$, we have

$$M_n^{-1} \mathbb{V}_{row}(B) M_n^{-1} = M_0^{-1} M_0 M_0^{-1} + X^\top V^{-1} V V^{-1} X = M_0^{-1} + X^\top V^{-1} X = M_n^{-1}. \quad (\text{S18})$$

This implies $\mathbb{V}_{row}(B) = M_n$. The mean follows from

$$M_n^{-1} \mathbb{E}[B] = A_1 \mathbb{E}[Z] + A_2 \mathbb{E}[Y_{rep}] = M_0^{-1} M_0 m_0 + X^\top V^{-1} Y = m_n, \quad (\text{S19})$$

and we obtain $\mathbb{E}[B] = M_n m_n$. Therefore, we can derive the next equality in distribution between B and the posterior distribution of the regression coefficient β as

$$B \stackrel{d}{=} \beta \mid \mathcal{D}, \Sigma \sim \text{MN}(M_n m_n, M_n, \Sigma). \quad (\text{S20})$$

This implies we can sample from $\beta \mid \mathcal{D}, \Sigma$ by solving a linear system. Specifically, by simply drawing samples from Z and Y_{rep} , we obtain a sample from $\beta \mid \mathcal{D}, \Sigma$ by solving the system $(M_0^{-1} + X^\top V^{-1} X)B = (M_0^{-1} Z + X^\top V^{-1} Y_{rep})$ for B . This approach is particularly advantageous for Bayesian transfer learning, as it avoids storing several large matrices when computing the posterior of $\beta \mid \mathcal{D}, \Sigma$. Instead, only the prior precision matrix for β , M_0^{-1} , and the product matrix $X^\top V^{-1}$ need to be stored, significantly reducing the memory footprint.

S5 Simulations for multivariate models

We supplement empirical results from Section 4; for further details, we refer to the main article. The current section follows this structure: we begin by comparing the computational performances of the double Bayesian predictive stacking (DBPS) approach with the multivariate spatial meta-kriging (MSMK [Guhaniyogi and Banerjee, 2019](#)), the linear model of coregionalization (LMC [Finley et al., 2015](#)), and the seemingly unrelated BART model

(suBART [Esser et al., 2025](#)), and conclude with empirical investigations for data partition dimension sensitivity for the DOUBLE BPS.

S5.1 Simulation - Computational performance

We investigate running times of our framework using two synthetic datasets with common structures but distinct sizes. Both datasets consist of $p = 2$ predictors and $q = 2$ response variables, but different numbers of spatial locations, $n = 5,000$ and $n = 10,000$, respectively. We generate and fix spatial coordinates from a uniform distribution on the unit square $([0, 1]^2)$. We build the $n \times n$ spatial correlation matrix V over these coordinates using $\rho_\phi(s_i, s_j) = \exp(-\phi\|s_i - s_j\|)$ with $\phi = 4$ and specify $\Sigma = \mathbb{I}_q$. From these specifications we generate the $n \times q$ matrix Y from the first equation of [\(2.4\)](#) with fixed $p \times q$ matrix $\beta = \begin{bmatrix} -0.75 & 1.85 \\ 0.90 & -1.10 \end{bmatrix}$, a fixed $n \times p$ matrix X with a first column of ones, representing the intercept, and $p - 1$ columns of values randomly simulated from a uniform distribution on $[0, 1]$ (emulating standardized predictors), and the proportion of spatial variability $\alpha = 0.8$.

For distributed learning approaches, i.e., DOUBLE BPS and MSMK, we perform the analyses in two settings: (i) $K = 10$ and $n = 5,000$; (ii) $K = 10$ and $n = 10,000$; (iii) $K = 5$ and $n = 5,000$; and (iv) $K = 20$ and $n = 10,000$. These settings produce subsets of size $n/K \in \{500, 1000\}$. We implement DOUBLE BPS using $J = 9$ candidate models $\mathcal{M}_j, j = 1, \dots, J$, where each model is specified by a set of candidate values for the hyperparameters α_j, ϕ_j in [\(2.4\)](#). These hyperparameters represent the proportion of spatial variability and the parameter(s) of the spatial correlation function, respectively. The set of candidate models is constructed as the set of all possible combinations of values for these hyperparameters. In the subsequent experiments, the grid of models was built using $\alpha \in \{0.70, 0.80, 0.90\}$ and $\phi \in \{3, 4, 5\}$. These values resemble an effective spatial range of $\{0.99, 0.75, 0.60\}$ units, corresponding to 70%, 53%, 42% of the maximum inter-site distance inside the unit square, beyond which the spatial correlation drops below 0.05. Equation [\(2.5\)](#)

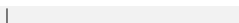
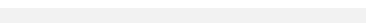
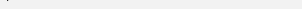
Setting	Model	Time (min)	Relative to BPS	Visual
$n = 5000, K = 10$	DBPS	1.38	1.0×	
	MSMK	51.41	37.3×	
$n = 5000, K = 5$	DBPS	7.22	1.0×	
	MSMK	237.23	32.9×	
$n = 5000$	DBPS	1.38 – 7.22	1.0 – 1.0×	 – 
	LMC	8975.31	>1000×	
	suBART	215.67	29 – 156×	 – 
$n = 10000, K = 20$	DBPS	2.24	1.0×	
	MSMK	103.36	46.1×	
$n = 10000, K = 10$	DBPS	10.58	1.0×	
	MSMK	446.01	42.2×	
$n = 10000$	DBPS	2.24 – 10.58	1.0 – 1.0×	 – 
	LMC	–	–	–
	suBART	557.60	53 – 249×	 – 

Table S2: Running times (in minutes), relative to DOUBLE BPS. Bars give a visual impression of time cost (where applicable).

follows choices in [Zhang et al. \(2021\)](#). Specifically, we set $m_0 = 0_{p \times q}$, $M_0 = 10\mathbb{I}_p$, $\Psi_0 = \mathbb{I}_q$, and $\nu_0 = 3$ in the MNIW joint prior for $\{\gamma, \Sigma\}$ in [2.5](#). For data analysis, we use an exponential spatial correlation function for $\rho_\phi(\cdot, \cdot)$, which is completely defined conditionally on \mathcal{M}_j , since specifies a value for ϕ . Again, in the conjugate framework, we draw $R = 250$ posterior samples used for inference.

We also apply MSMK to the two simulated datasets with the same combinations of n and K as DOUBLE BPS. Unlike DOUBLE BPS, where we stack analytically tractable posteriors over a range of fixed values of spatial covariance kernel parameters, the MSMK implementation attempts full Bayesian inference using prior distributions on spatial covariance kernel parameters. We fit the linear model of coregionalization described in [Finley et al. \(2015\)](#) for each subset of the multivariate spatial data using MCMC. The posterior samples from the K subsets are combined using Weiszfeld’s iterative algorithm ([Minsker et al., 2017](#)) to produce an estimate of the geometric median of the posterior distributions. For both experimental settings, we then fit LMC, and suBART on the full dataset, where they were endowed with default prior settings, following [Finley et al. \(2015\)](#), and [Esser et al. \(2025\)](#), respectively.

Table [S2](#), which compares the computational speed of DOUBLE BPS with other considered approaches reveals massive computational gains accrued from DOUBLE BPS. The computational advantage evinced from the relative ratio becomes more pronounced as the size of the

data becomes larger, despite the larger subsets. This is explained by the fact that fitting the Gaussian process regression dominates the computation relative to the assimilation of inference from the subsets. If the number of locations explode, then the geometric median of posteriors required by MSMK is computationally unfeasible. While MSMK offers Bayesian estimates using MCMC for each subset, DOUBLE BPS avoids MCMC and, hence, issues of convergence. Similar arguments follow for LMC and subBART. As expected, the linear model of coregionalization, when fitted on the entire set of locations, gives a disastrous performance, taking almost a week of computation in the lighter simulation settings, and makes it infeasible to record results for $n = 10,000$. Notwithstanding the scalability offered by this multivariate extension of the Bayesian additive regression model, the subBART does not have any chance to provide inference in a comparable time.

Figure S4, which depicts estimated response surfaces using DOUBLE BPS and MSMK corresponding to $n = 5000$ and $K = 10$, shows that inferences are practically indistinguishable. The root mean squared prediction error (RMSPE), reported in Figure S4, denotes the average squared differences between the generated and estimated values of the response and reveals minor discrepancies between DOUBLE BPS and MSMK. Section S5 presents results for the other configurations of n and K , each of which reveals that DOUBLE BPS offers practically indistinguishable spatial interpolation from MSMK at a fraction of the computational cost.

Figure S5 reports 95% posterior predictive intervals for the response. Again, the empirical coverage is impressive. While we see slightly wider intervals from DOUBLE BPS, this is less pronounced than the underestimation of variability seen with MSMK. Moreover, Figure S5 reveals superior MAP estimates for the DOUBLE BPS. Finally, Figure S6 presents the recovery of parameter estimates. As seen in predictive inference, the posterior credible intervals for parameters also deliver practically indistinguishable inference for the two modeling frameworks. In particular, both methods recover the true values for β and Σ , while DOUBLE BPS reconstructs a better point estimate for range parameters ϕ using $\sum_{k=1}^K \hat{w}_k \sum_{j=1}^J \hat{z}_j \phi_j$.

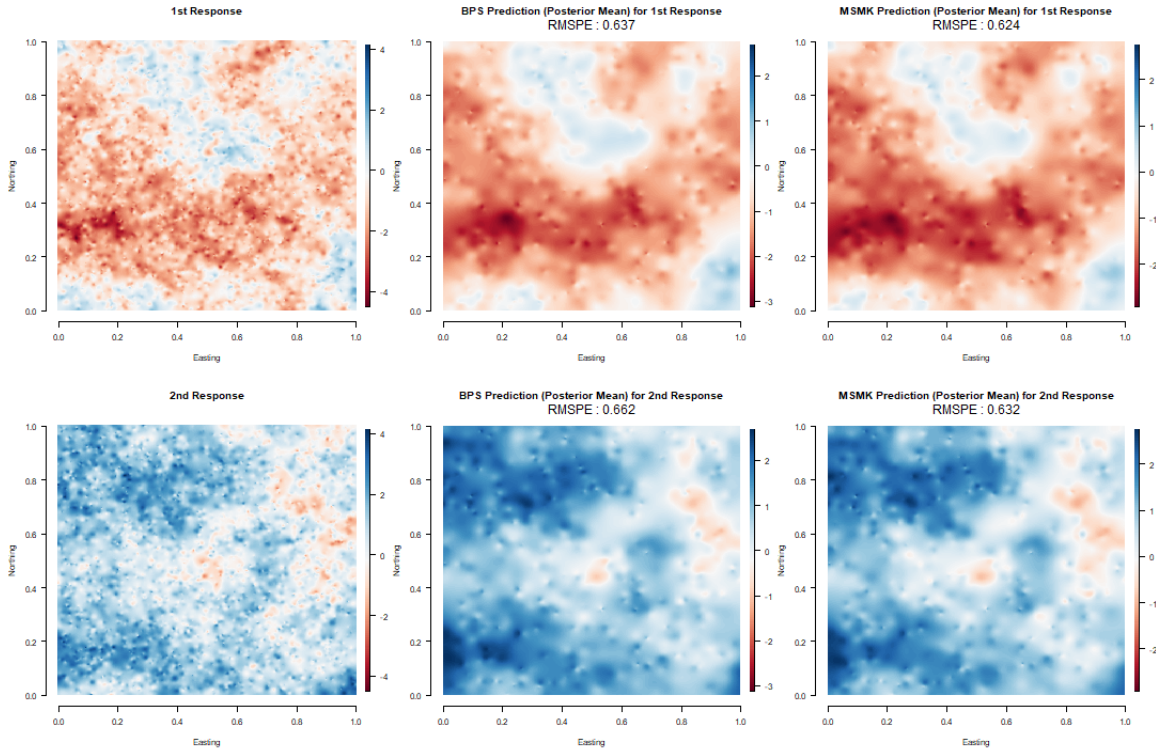


Figure S4: from left to right: comparison between the true generated response surfaces, the surfaces predicted from **DOUBLE BPS** and **MSMK** (posterior mean), with RMSPE. For $n = 5000$, $K = 10$.

Figure S7 shows the estimated response surface using DOUBLE BPS for $\{n = 5000, K = 5\}$. This plot reveals no noteworthy differences compared to the results obtained from MSMK. Although the RMSPE values for MSMK are slightly better, the differences are negligible when compared with the response scale, leading us to conclude that both approaches exhibit almost identical predictive performance. Regarding the first scenario from Section S5.1, it is unsurprising that a doubled number of locations per partition leads to improved performance. Figure S9 provides empirical support to this. While MSMK shows some degree of spatial over-smoothing, as indicated by higher estimated values of ϕ compared to the true ones, DOUBLE BPS does not exhibit such deviations. Both the MAP estimates and the posterior inferences for DOUBLE BPS show strong performance.

Figure S8 aligns with the previous conclusions, highlighting slightly wider predictive credibility intervals for DOUBLE BPS compared to MSMK. However, this difference is less pronounced than the underestimation of variability witnessed with MSMK. For both approaches, the empirical coverage appears impressive.

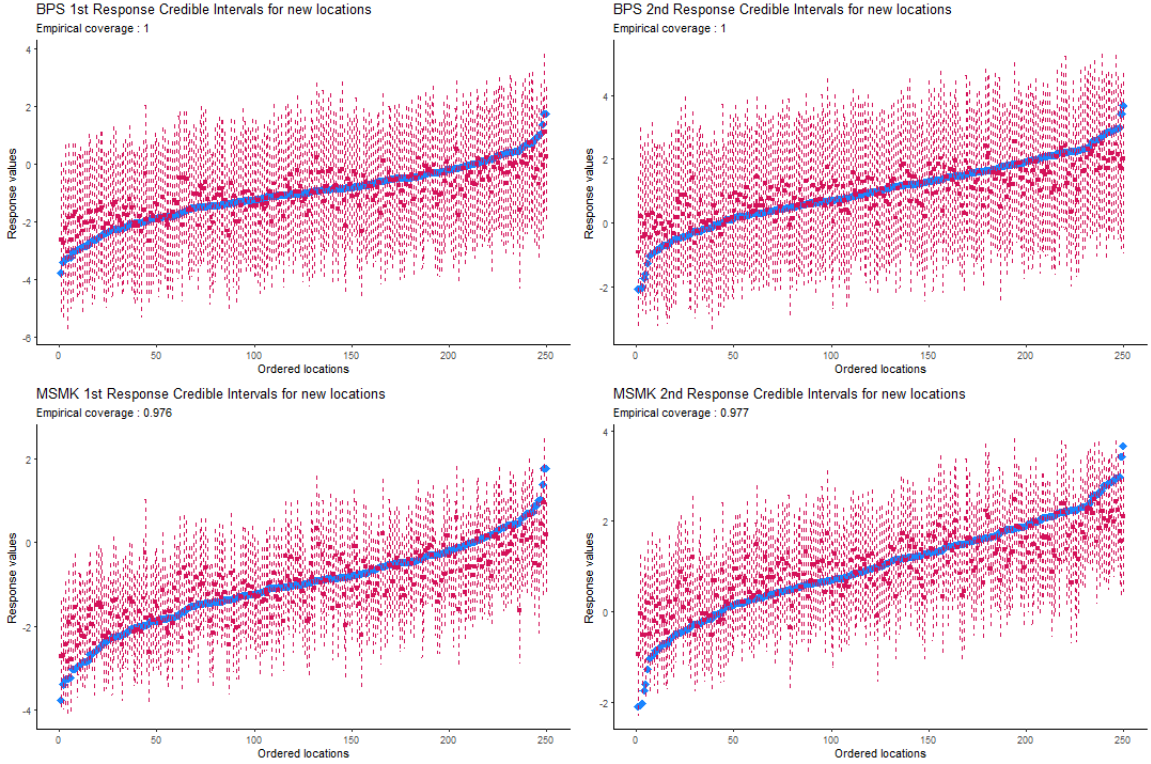


Figure S5: from top to bottom: comparison between posterior predictive intervals for the predicted response from DOUBLE BPS and MSMK, with empirical coverage. For $n = 5000$, $K = 10$.

Despite focusing on the larger dataset later in this section, where $n = 10,000$, the results increasingly appear to depend on the size of the subsets rather than the number of partitions. This remark on the influence of local inferences on global performance, with the number of partitions playing a lesser role.

For the case $\{n = 10,000, K = 20\}$, Figure S10 compares the estimated posterior mean surfaces. The performances of DOUBLE BPS and MSMK are nearly equivalent. The most noticeable difference is in Figure S11, where MSMK produces narrower predictive credible intervals for the response variable. However, in Figure S6, DOUBLE BPS demonstrates superior posterior MAP estimates, including for the range parameters, which are typically challenging to identify. Together, Figures S11, S12, and S10 present comparable findings to the $\{n = 5,000, K = 10\}$ setting, reinforcing the importance of subset learning over the overall dataset size, as expected.

The simulation experiment concludes with the $\{n = 10,000, K = 10\}$ setting. Once again, Figures S13, S14, and S15 show results consistent with previous settings, particularly

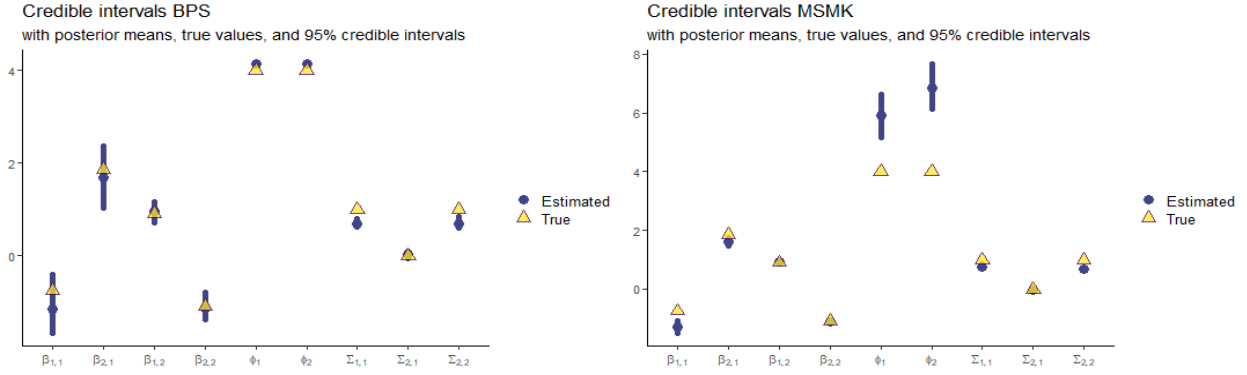


Figure S6: from left to right: comparison between posterior credible intervals for the parameters recovered from **DOUBLE BPS** and **MSMK**. For $n = 5000$, $K = 10$.

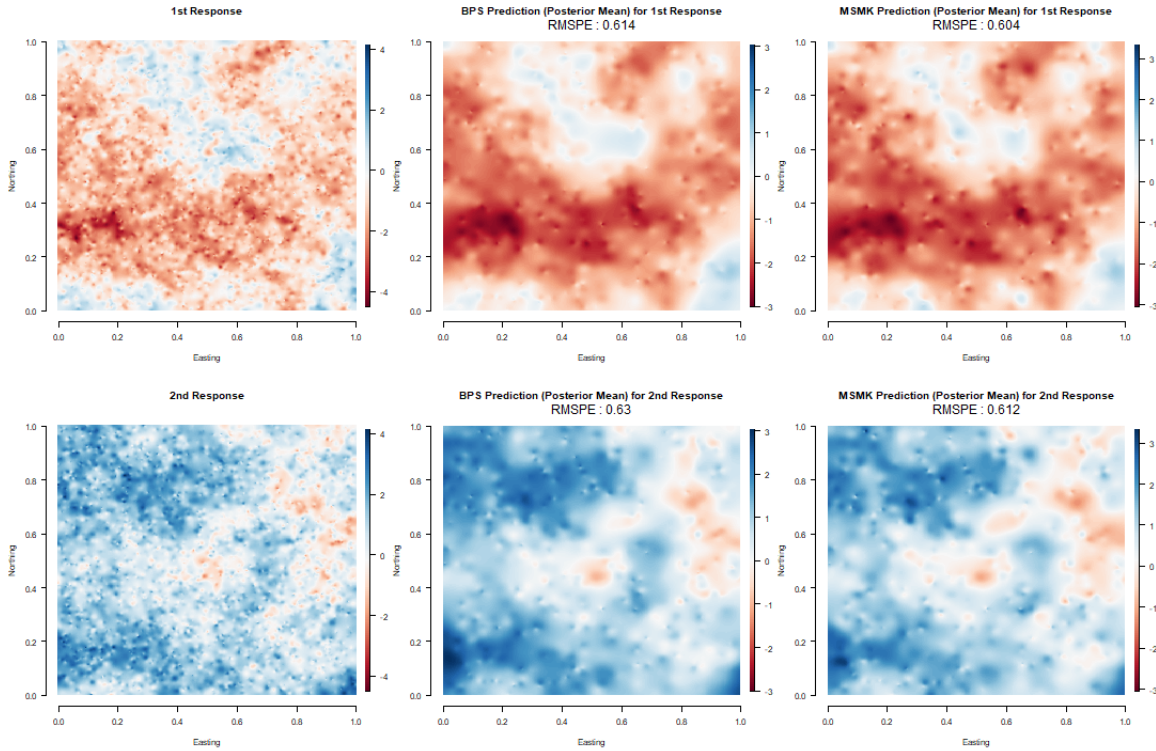


Figure S7: from left to right: comparison between the true generated response surfaces, the surfaces predicted from **DOUBLE BPS** and **MSMK** (posterior mean), with RMSPE. For $n = 5000$, $K = 5$.

with $\{n = 5,000, K = 10\}$, highlighting the critical role of partition size in achieving reliable posterior inferences. In Figure S15, despite the strong posterior performance, **DOUBLE BPS** exhibits wider posterior credible intervals compared to **MSMK**. This is similarly reflected in Figure S14, where **DOUBLE BPS** achieves empirical coverage of 100% for the 95% predictive intervals. Furthermore, **DOUBLE BPS** tends to avoid the underestimation of spatial variances in Σ , as evidenced in Figure S15, supporting earlier findings.

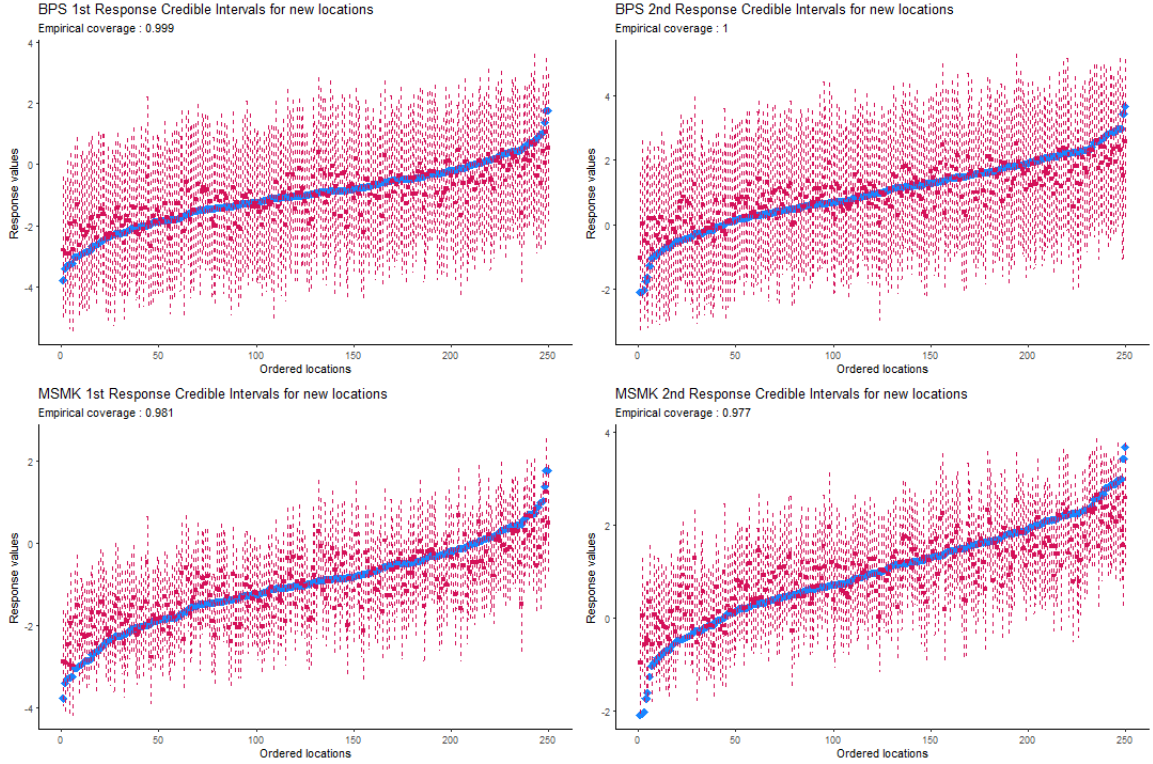


Figure S8: from top to bottom: comparison between posterior predictive intervals for the predicted response from DOUBLE BPS and MSMK, with empirical coverage. For $n = 5000$, $K = 5$.

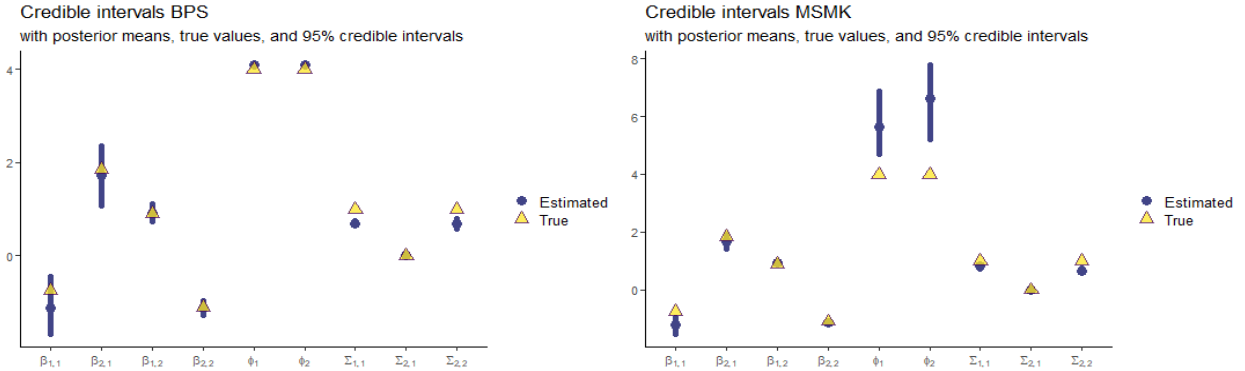


Figure S9: from left to right: comparison between posterior credible intervals for the parameters recovered from DOUBLE BPS and MSMK. For $n = 5000$, $K = 5$.

In conclusion, notwithstanding indistinguishable posterior inferences between DOUBLE BPS and multivariate SMK, Table S2 clearly illustrates that the primary advantage of Bayesian predictive stacking lies in its enormous computational efficiency. This speedup is crucial for delivering feasible Bayesian inference for large datasets within GeoAI systems.

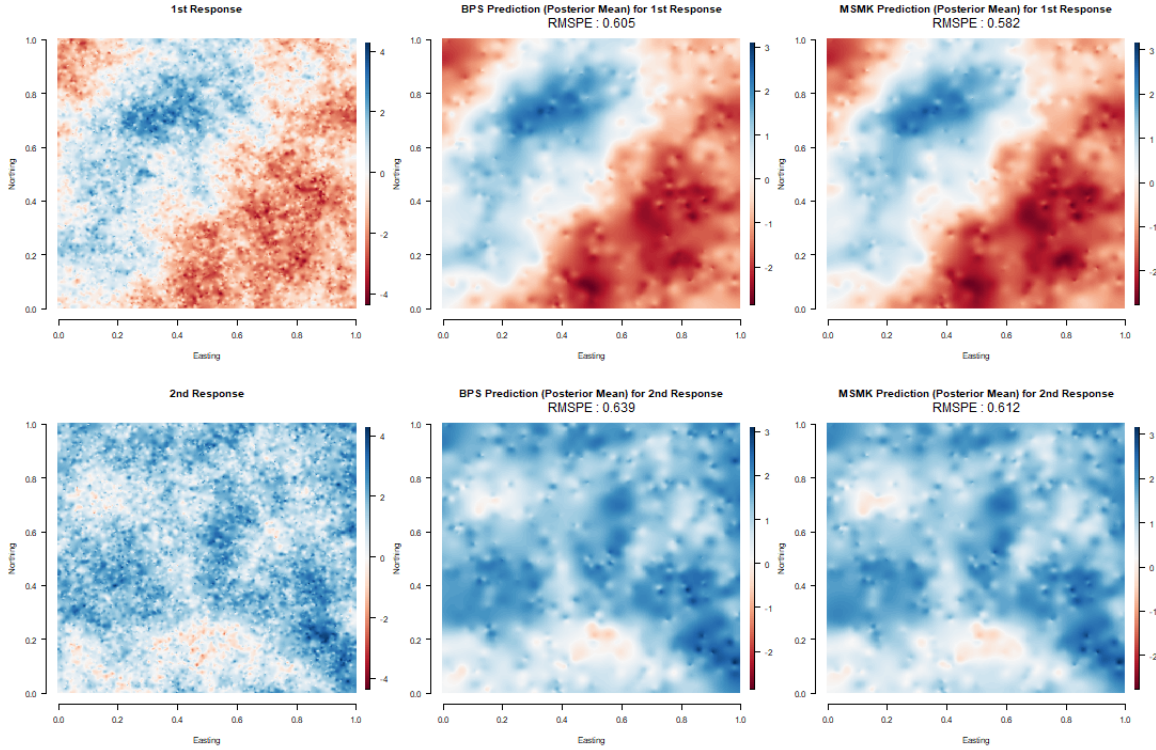


Figure S10: from left to right: comparison between the true generated response surfaces, the surfaces predicted from DOUBLE BPS and MSMK (posterior mean), with RMSPE. For $n = 10000$, $K = 20$.

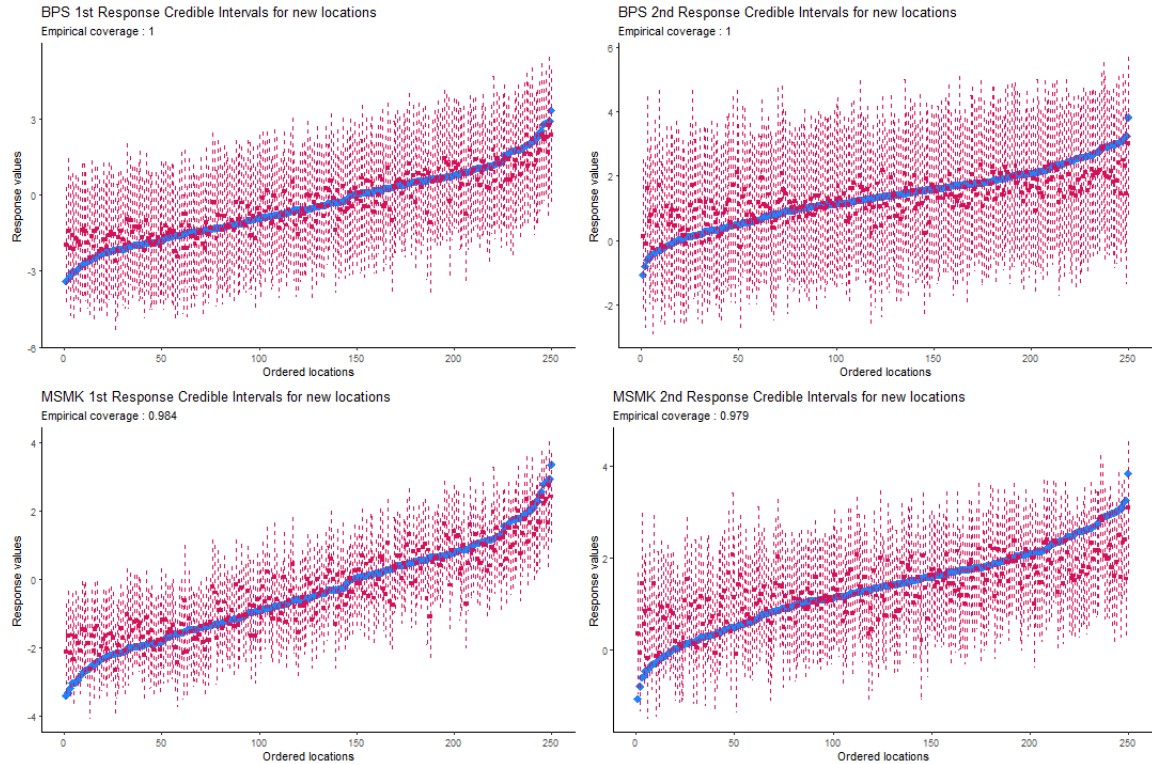


Figure S11: from top to bottom: comparison between posterior predictive intervals for the predicted response from DOUBLE BPS and MSMK, with empirical coverage. For $n = 10000$, $K = 20$.

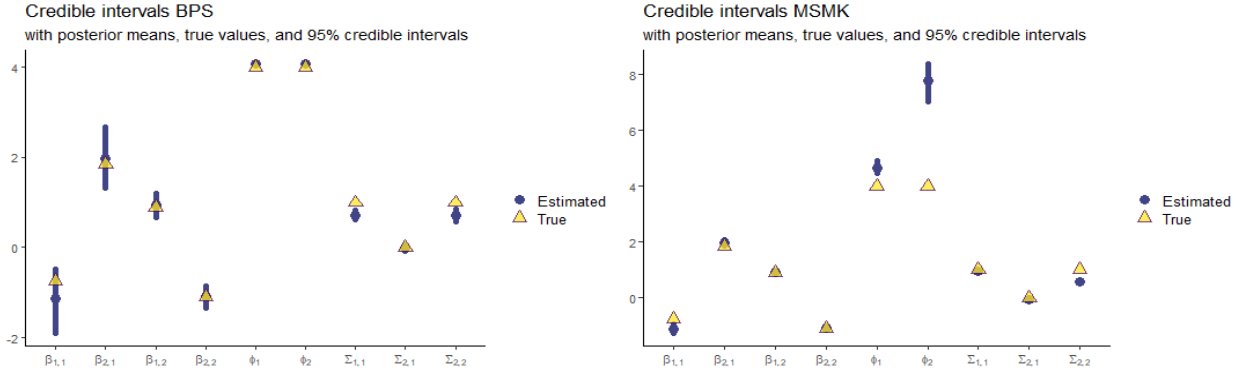


Figure S12: from left to right: comparison between posterior credible intervals for the parameters recovered from **DOUBLE BPS** and **MSMK**. For $n = 10000$, $K = 20$.

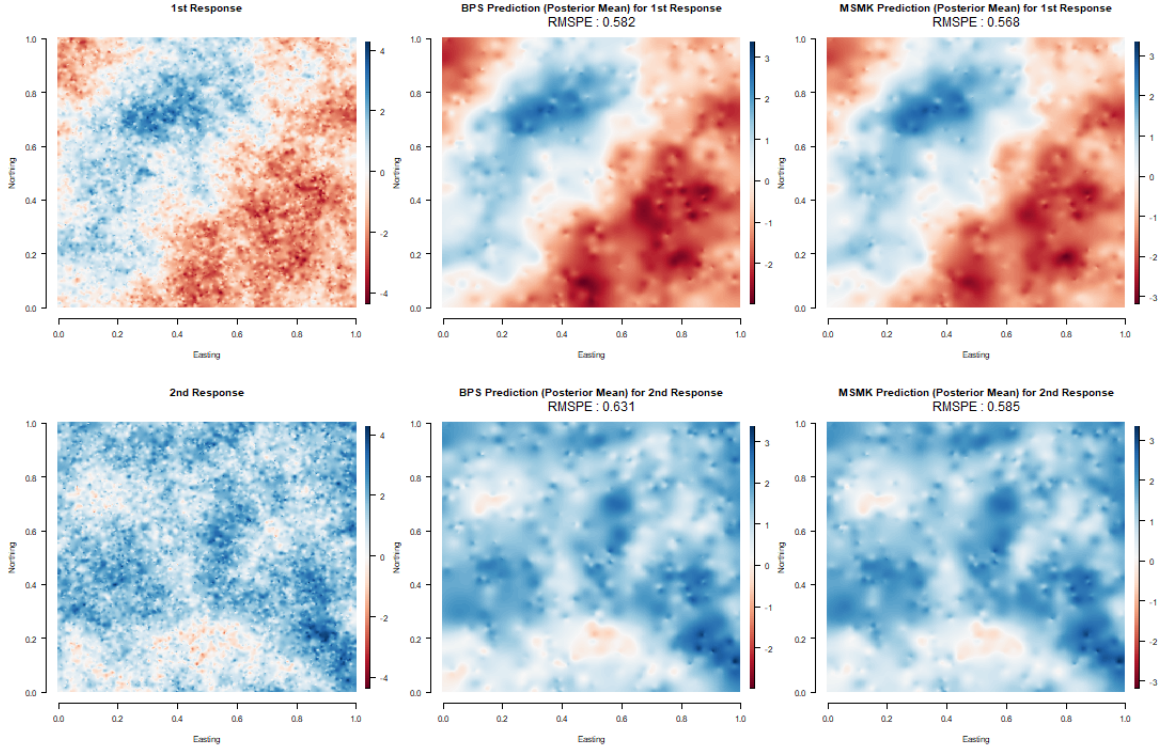


Figure S13: from left to right: comparison between the true generated response surfaces, the surfaces predicted from **DOUBLE BPS** and **MSMK** (posterior mean), with **RMSPE**. For $n = 10000$, $K = 10$.

S5.2 Simulation - Subset size sensitivity

The methodological novelty introduced in Section 2.3 can be summarized in three main steps, as illustrated in Figure 1. First, we partition the original, often massive, dataset into K smaller subsets. The number of locations in each partition is a critical decision, seriously impacting inferential, predictive, and computational outcomes. Accordingly, a trade-off arises between computational resources and performance.

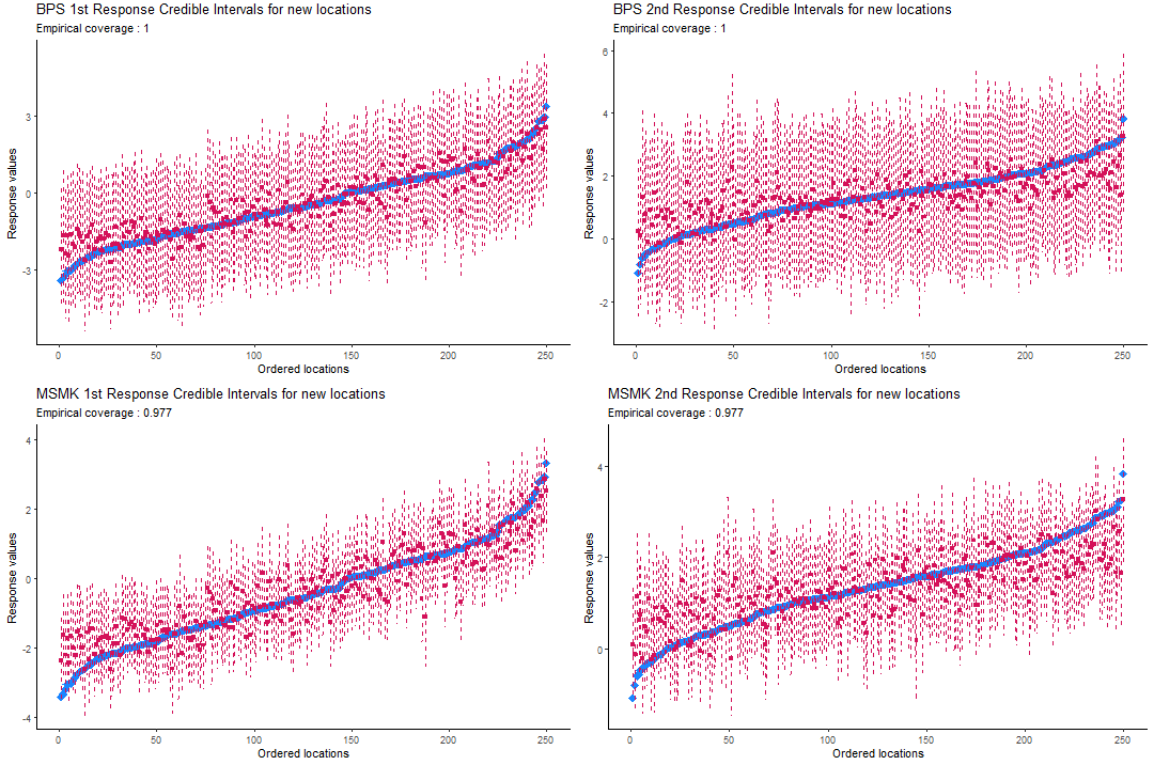


Figure S14: from top to bottom: comparison between posterior predictive intervals for the predicted response from DOUBLE BPS and MSMK, with empirical coverage. For $n = 10000$, $K = 10$.

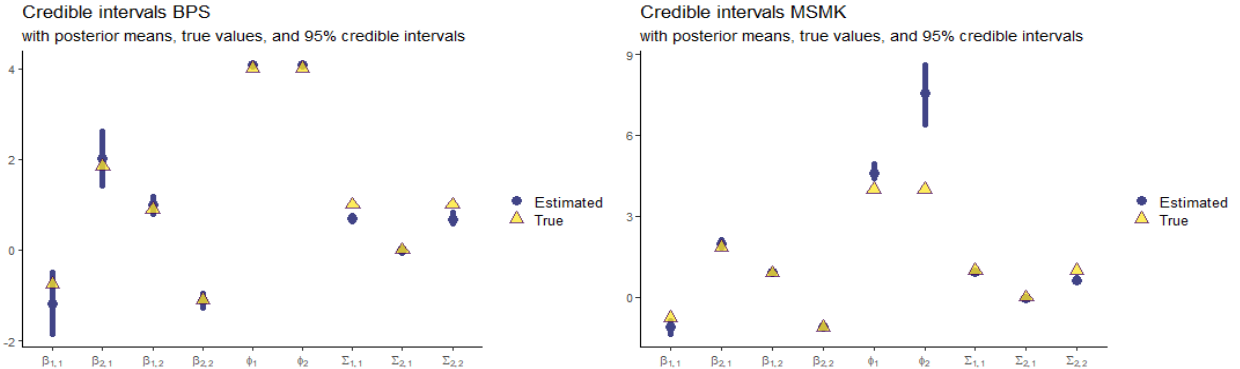


Figure S15: from left to right: comparison between posterior credible intervals for the parameters recovered from DOUBLE BPS and MSMK. For $n = 10000$, $K = 10$.

To address this, we conduct a simulation analysis to assess the sensitivity of the results to subset size. This section aims to investigate how predictive performance (in terms of RMSPE), and runtime (in seconds) change as the number of locations within each partition grows. Intuitively and theoretically, as the dimension of the subsets grows, we expect predictive performance to improve, while runtime increases polynomially with n . To enhance the comparability of the results, we apply min-max normalization to each variable, defined as

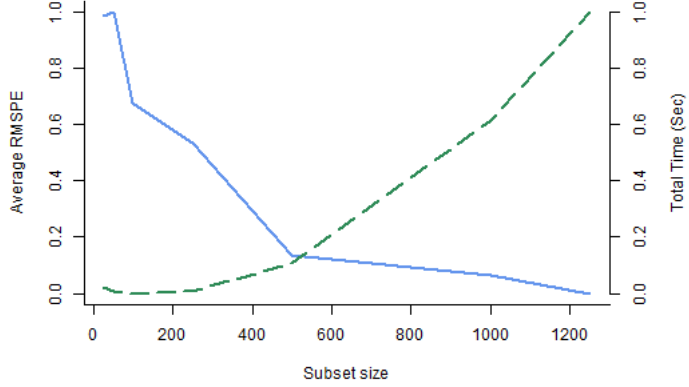


Figure S16: Comparison between average RMSPE (solid line) and model fitting time (dashed line) across various subset dimensions (both min-max normalized).

$\tilde{x} = \frac{x - \min(x)}{\max(x) - \min(x)}$. This normalization scales all variables to the interval $[0, 1]$, facilitating a more direct graphical comparison.

We utilize a multivariate synthetic dataset comprising $n = 5,000$ locations, $q = 2$ simulated responses, and $p = 2$ predictors to explore the sensitivity to subset size. This dataset is generated from the model in Equation (2.4), with parameters $\beta = \begin{bmatrix} -0.75 & 1.85 \\ 0.90 & -1.10 \end{bmatrix}$ and $\Sigma = \begin{bmatrix} 1.00 & -0.30 \\ -0.30 & 1.00 \end{bmatrix}$. The predictor matrix X includes an intercept and $p - 1$ columns generated from a standard uniform distribution over $[0, 1]$. The range parameter for the exponential spatial covariance function, and the proportion of spatial variability, are fixed at $\phi = 4$ and $\alpha = 0.8$ respectively. We set prior information as follows: $m_0 = 0_{p \times q}$, $M_0 = 10\mathbb{I}_p$, $\Psi_0 = \mathbb{I}_q$, and $\nu_0 = 3$. These specifications and prior information remain constant, allowing only the number of locations in each subset to vary. In performing DOUBLE BPS detailed in Section 2.3, we consider $J = 9$ competitive models characterized by $\alpha \in \{0.70, 0.80, 0.90\}$ and $\phi \in \{3, 4, 5\}$.

We focus our sensitivity analysis by selecting the following set of partition sizes: $\{25, 50, 100, 250, 500, 1000, 1250\}$, which correspond to the number of partitions $K \in \{200, 100, 50, 20, 10, 5, 4\}$. Figure S16 illustrates the two curves resulting from this sensitivity analysis.

As anticipated, the behavior of the two curves aligns with theoretical expectations across most scenarios. Specifically, the total time required to fit the model increases monotonically,

exhibiting more than linear growth in the number of locations within each partition, as the dashed line exhibits in Figure S16. Conversely, the root mean square prediction error experiences an unexpected fluctuation, likely due to the extremes of very low or high numbers of locations/subsets (50/100). RMSPE decreases until it stabilizes at a “plateau” for partition sizes of 500 units on. The trends observed in Figure S16 reveal a compromise between predictive performance and computational effort close to a subset size of 500 units.

However, Figure S16 also raises an important question: how much predictive error is acceptable? The two quantities, although normalized for comparison, differ significantly in their scales. More precisely, the trade-off is asymmetric: doubling the number of locations per partition yields a moderate reduction in RMSPE, while the runtime can increase dramatically, rising at least quadratically with n . For all these reasons, we generally opt for a subset size of 500 locations in both our simulation studies and data applications. Nonetheless, we should not overlook the opportunity to reduce this size, accepting a trade-off in predictive performance to achieve even faster global Bayesian inference for exceptionally large GeoAI applications.

References

CVX Research, I. (2012, August). CVX: Matlab software for disciplined convex programming, version 2.0.

Esser, J., M. Maia, A. C. Parnell, J. Bosmans, H. v. Dongen, T. Klausch, and K. Murphy (2025, February). Seemingly unrelated Bayesian additive regression trees for cost-effectiveness analyses in healthcare. arXiv:2404.02228 [stat].

Finley, A. O., S. Banerjee, and A. E. Gelfand (2015). spbayes for large univariate and multivariate point-referenced spatio-temporal data models. *Journal of Statistical Software* 63(13), 1–28.

Fu, A. and B. Narasimhan (2023). *ECOSolver: Embedded Conic Solver in R*. R package version 0.5.5.

Fu, A., B. Narasimhan, and S. Boyd (2020). Cvxr: An r package for disciplined convex optimization. *Journal of Statistical Software* 94(14), 1–34.

Grant, M. C. (2005). *Disciplined convex programming*. Ph. D. thesis.

Guhaniyogi, R. and S. Banerjee (2018). Meta-kriging: Scalable bayesian modeling and inference for massive spatial datasets. *Technometrics* 60(4), 430–444.

Guhaniyogi, R. and S. Banerjee (2019, May). Multivariate spatial meta kriging. *Statistics & Probability Letters* 144, 3–8.

Gupta, A. K. and D. K. Nagar (2000). *Matrix variate distributions*. Monographs and surveys in pure and applied mathematics. Boca Raton: Chapman & Hall/CRC.

Iranmanesh, A., M. Arashi, and S. M. M. a. Tabatabaey (2010). On conditional applications of matrix variate normal distribution. *Iranian Journal of Mathematical Sciences and Informatics* 5(2), 33–43.

Minsker, S., S. Srivastava, L. Lin, and D. B. Dunson (2017). Robust and scalable bayes via a median of subset posterior measures. *Journal of Machine Learning Research* 18(124), 1–40.

O'Donoghue, B., E. Chu, P. Neal, and S. Boyd (2016, Jun). Operator splitting for conic optimization via homogeneous self-dual embedding. *Journal of Optimization Theory and Applications* 169(3), 1042–1068.

Sellers, P. J. (1985, August). Canopy reflectance, photosynthesis and transpiration. *International Journal of Remote Sensing* 6(8), 1335–1372. Publisher: Taylor & Francis _eprint: <https://doi.org/10.1080/01431168508948283>.

Tucker, C. J. (1979, May). Red and photographic infrared linear combinations for monitoring vegetation. *Remote Sensing of Environment* 8(2), 127–150.

Yao, Y., A. Vehtari, D. Simpson, and A. Gelman (2018). Using Stacking to Average Bayesian Predictive Distributions (with Discussion). *Bayesian Analysis* 13(3), 917–1007.

Zhang, L., S. Banerjee, and A. O. Finley (2021). High-dimensional multivariate geostatistics: A bayesian matrix-normal approach. *Environmetrics* 32(4), e2675.